Acta Geologica Sinica (English Edition), 2019, 93(5): 1434–1455

Recognition of Early Paleozoic Magmatisms in the Supposed Proterozoic Basements of Zhalantun, Great Xing'an Range, NE China

QIN Tao[1, 2], GUO Rongrong[3, *], ZANG Yanqing[2], QIAN Cheng[2], WANG Yan[2], SI Qiuliang[2], SUN Wei[2] and MA Yongfei[2]

[1] *College of Earth Sciences, Jilin University, Changchun 130061, China*
[2] *Shenyang Institute of Geology and Mineral Resources, Shenyang 110034, Liaoning, China*
[3] *Key Laboratory of Ministry of Education on Safe Mining of Deep Metal Mines, Department of Geology, Northeastern University, Shenyang 110819, China*

Abstract: The Zhalantun terrane from the Xing'an massif, northeast China, was used to be considered as Proterozoic basements. However, amounts of detrital zircon ages from the meta-sedimentary rocks deny the existence of Precambrian basements recently. Notably, magmatic rocks were barely reported to limit the exact ages of the Zhalantun basements. In this study, we collected rhyolite, gabbro and quartz diorite for zircon in-situ U-Pb isotopic dating, which yield crystallization ages of ~505 Ma, ~447 Ma and ~125 Ma, respectively. Muscovite schist and siltstone define maximum depositional ages of ~499 Ma and ~489 Ma, respectively. Additionally, these dated supracrustal rocks and plutons also yield ancient detrital/xenocryst zircon ages of ~600–1000 Ma, ~1600–2220 Ma, ~2400 Ma, ~2600–2860 Ma. Based on the whole-rock major and trace element compositions, the ~505 Ma rhyolites display high SiO_2 and alkaline contents, low Fe_2O_{3T}, TiO_2 and Al_2O_3, and relatively high MgO and $Mg^{\#}$, which exhibit calc-alkaline characteristics. These rhyolites yield fractionated REE patterns and negative Nb, Ta, Ti, Sr, P and Eu anomalies and positive Zr anomalies. The geochemistry, petrology and Lu-Hf isotopes imply that rhyolites were derived from the partial melting of continental basalt induced by upwelling of sub-arc mantle magmas, and then experienced fractional crystallization of plagioclase, which points to a continental arc regime. The ~447 Ma gabbros exhibit low SiO_2 and alkaline contents, high Fe_2O_{3T}, TiO_2, MgO and $Mg^{\#}$. They show minor depletions of La and Ce, flat MREE and HREE patterns, and negative Nb, Ta, Zr and Hf anomalies. Both sub-arc mantle and N-MORB-like mantle were involved in the formation of the gabbros, indicative of a probable back-arc basin tectonic setting. Given that, the previously believed Proterozoic supracrustal rocks and several plutons from the Zhalantun Precambrian basements were proved to be Paleozoic to Mesozoic rocks, among which these Paleozoic magmatic rocks were generally related to subduction regime. So far, none Proterozoic rocks have been identified from the Zhalantun Precambrian basement, though some ~600–3210 Ma ancient detrital/xenocryst zircons were reported. Combined with ancient zircon ages and newly reported ~2.5 Ga and ~1.8 Ga granites from the south of the Zhalantun, therefore, the Precambrian rocks probably once exposed in the Zhalantun while they were re-worked and consumed during later long tectonic evolutionary history, resulting in absence of Precambrian rocks in the Zhalantun.

Key words: early Paleozoic magmatism, Xinghuadukou Group, Jiageda Formation, Zhalantun terrane, Great Xing'an Range, Central Asian Orogenic Belt

Citation: Qin et al., 2019. Recognition of Early Paleozoic Magmatisms in the Supposed Proterozoic Basements of Zhalantun, Great Xing'an Range, NE China. Acta Geologica Sinica (English Edition), 93(5): 1434–1455. DOI: 10.1111/1755-6724.14359

1 Introduction

The Central Asian Orogenic Belt (CAOB) is located between the Siberian Craton, North China Craton and Tarim Craton, and consists of a collage of micro-continental blocks and accretionary orogenic belts (Sengör et al., 1993; Jahn et al., 2000; Ge et al., 2007; Xu et al., 2009; Li et al., 2016, 2013; Xiao and Santosh, 2014; Wang., L.M., 2015; Dong et al., 2016; Li et al., 2017). Northeastern China (NE China) lies in the eastern segment of CAOB and was dominated by three tectonic domains: (i) the Paleo-Asian Ocean tectonic domain during the Late Paleozoic which resulted in several micro-continental massifs separated by E-W trending suture zones (Sengör et al., 1993; Xu et al., 2013a; Wilde and Zhou, 2015; Pei et al., 2016); (ii) the Mongol-Okhotsk suture zone triggered by final collision between the Siberia Craton and NE China blocks during the Late Jurassic to Early Cretaceous (Xu et al., 2013b; Khanchuk et al., 2015; Liu et al., 2017), and (iii) the circum-Pacific tectonic domain that dominated the NE China since the Early Mesozoic (Wu et al., 2003a, b, 2011; Xu et al., 2013a, b, c; Wang et al., 2015a).

NE China is composed of Paleozoic massifs that are

* Corresponding author. E-mail: guorongrong@mail.neu.edu.cn

Erguna, Xing'an, Songnen and Jiamusi-Khanka massifs from northwest to southeast (Feng et al., 2018, 2015; Dong et al., 2016; Liu et al., 2017; Li et al., 2018; Xu et al., 2019). Crystalline metamorphic massifs within the NE China are generally considered as fragments disassembled from major Precambrian cratons (Kozakov et al., 2007; Kröner et al., 2011), which contain Precambrian records. For example, the Zhalantun terrane has been regarded as Precambrian basements in the Xing'an massif, and comprises Proterozoic Xinghuadukou Group and Jiageda Formation (Cui et al., 2015; Zhou et al., 2014; Ren et al., 1999; Yang, 2007). The 1:250 000 Zhalantun regional geological survey report (RGS, He et al., 2006) further recognized Proterozoic intrusive rocks from the Zhalantun, which are ~1048 Ma monzodiorite and ~2096 Ma gabbro (single zircon U-Pb dilution method). Additionally, the ~1048 Ma monzodiorite intrudes the Xinghuadukou Group, further implying Proterozoic products of the Xinghuadukou Group (He et al., 2006). However, several Paleozoic ages have been documented from the supposed Proterozoic basements in the Zhalantun area and nearby (Yang et al., 2007; Miao et al., 2007; Zhou et al., 2015; Cui et al., 2015). For example, Yang (2007) reported the youngest age peak of chlorite schists and mica schists (metamorphic sedimentary rocks) from the Proterozoic basements of the Zhalantun were ~497–519 Ma (LA-ICPMS zircon U-Pb dating method). Miao et al. (2007) reported that chlorite schist (interpreted as meta-basic rock) from the Zhalantun Proterozoic basements crystallized at ~506 Ma (SHRIMP zircon U-Pb dating method). The mica schist and meta-sandstone from the southwestern Zhalantun gave the youngest detrital zircon ages of ~412–429 Ma (LA-ICPMS zircon U-Pb dating method, Cui et al., 2015). Collectively, some geologists purposed that these Proterozoic basements actually formed in the Early Paleozoic rather than Proterozoic era, and underwent later metamorphisms and deformations (Zhou et al., 2014; Liu et al., 2017; Xu et al., 2019). Though several Paleozoic ages have been reported from the Zhalantun basements in the past few years, most studies just focused on the metamorphic sedimentary rocks which can only limit maximum sedimentary ages rather than exact crystallization ages. Whereas, the magmatic rocks which can directly and convincingly define the formation age of the Zhalantun basement, are barely reported in the Zhalantun. Besides, some reported ages are questionable. For example, less than ten zircon grains selected from the reported Proterozoic ~1048 Ma gabbro and ~2096 Ma monzodiorite were dated by single zircon evaporation U-Pb method, which lack statistical significance.

In this study, we collected rhyolite, siltstone, muscovite schist, and reported Proterozoic gabbro and diorite from the Zhalantun basements for whole-rock geochemical, zircon U-Pb and Lu-Hf isotopic analyses, among which rhyolite, gabbro and diorite can limit the exact formation ages of the Zhalantun basements. Furthermore, by discussing petrogenesises for the rhyolite and gabbro, we try to determine the contemporaneous tectonic setting of the Zhalantun basements.

2 Geological Background

NE China, the eastern segment of the CAOB, comprises Erguna massif, Xing'an massif, Songnen-Zhangguangcai Rang massif and Jiamusi-Khanka massif from northwest to southeast which are separated by Xinlin-Xiguitu suture zone, Hegenshan-Nenjiang-Heihe suture zone and Mudanjiang fault (Fig. 1, Feng et al., 2015; Dong et al., 2016; Li et al., 2017, 2018; Liu et al., 2018).

The Xing'an massif is located between Erguna massif and Songnen basin. The Precambrian basements of the Xing'an massif are mainly distributed around Zhalantun, Woniuhe, Arongqi, Dabeigou and Lizishan areas, and have traditionally been named as Zhalantun Precambrian terrane by 1:250 000 Zhalantun RGS (He et al., 2006). Based on Rb-Sr and Sm-Nd isotopic dating methods and comparisons of regional stratum and petrography, the Zhalantun supracrustal rocks were named as the Paleoproterozoic Xinghuadukou Group and Neoproterozoic Jiageda Formation (or Xinkailing and Fengshuigouhe Groups by IMBGMR, 1991) that were parallel to those contemporaneous stratums of the Erguna massif (Miao et al., 2007). The Paleoproterozoic Xinghuadukou Group mainly comprises mica quartz schist, two-mica schist, chlorite quartz schist, chlorite actinolite schist and chlorite schist (IMBGMR, 1991; He et al., 2006; Yang et al., 2007). The Neoproterozoic Jiageda Formation is dominantly composed of slate, phyllite, two-mica schist, meta-sandstone and minor meta-volcanic rocks. Both Xinghuadukou Group and Jiageda Formation had undergone greenschist metamorphism with temperature of 380–420°C and pressure of ~0.4 Gpa (He et al., 2006). Except Proterozoic supracrustal rocks, the Zhalantun basements still consist of intrusive rocks, like ~2096 Ma gabbro in the Yalu area and ~1048 Ma monzodiorite in the Lingxi area (He et al., 2006). Monzodiorite was reported as a Neoproterozoic pluton intruding the Xinghuadukou Group, which was considered as a convincing evidence to prove that the Xinghuadukou Group was much older than the Neoproterozoic (He et al., 2006). In addition, the Zhalantun records multiple Mesozoic granitoids, volcanic rocks and clastic sedimentary rocks, like Manitu (J_3) and Baiyingaolao (K_1) Formations, as well as Paleozoic granitoids (e.g. Wu et al., 2011; Yang et al., 2015; Li et al., 2017; Liu et al., 2018).

3 Sample Description and Analytical Methods

3.1 Sample description

In this study, we collected rhyolite, muscovite schist and siltstone from the Xinghuadukou Group and Jiageda Formation in the Zhalantun area (Fig. 1), and supposed Proterozoic diorite and gabbro in the Zhalantun and Yalu areas. The detailed locations and mineral assemblages of the collected samples are listed in Table 1.

Five rhyolites (samples BAS03-1, BAS03-2, BAS03-3, BAS03-4, BAS03-5) were intruded by Paleozoic syenite (unpublished data). They exhibit porphyritic texture and weak rhyolitic structure, with phenocryst of quartz and matrix of quartz + feldspar (Fig. 2a and b). Minor amphibole is exposed as well, which is partially altered to

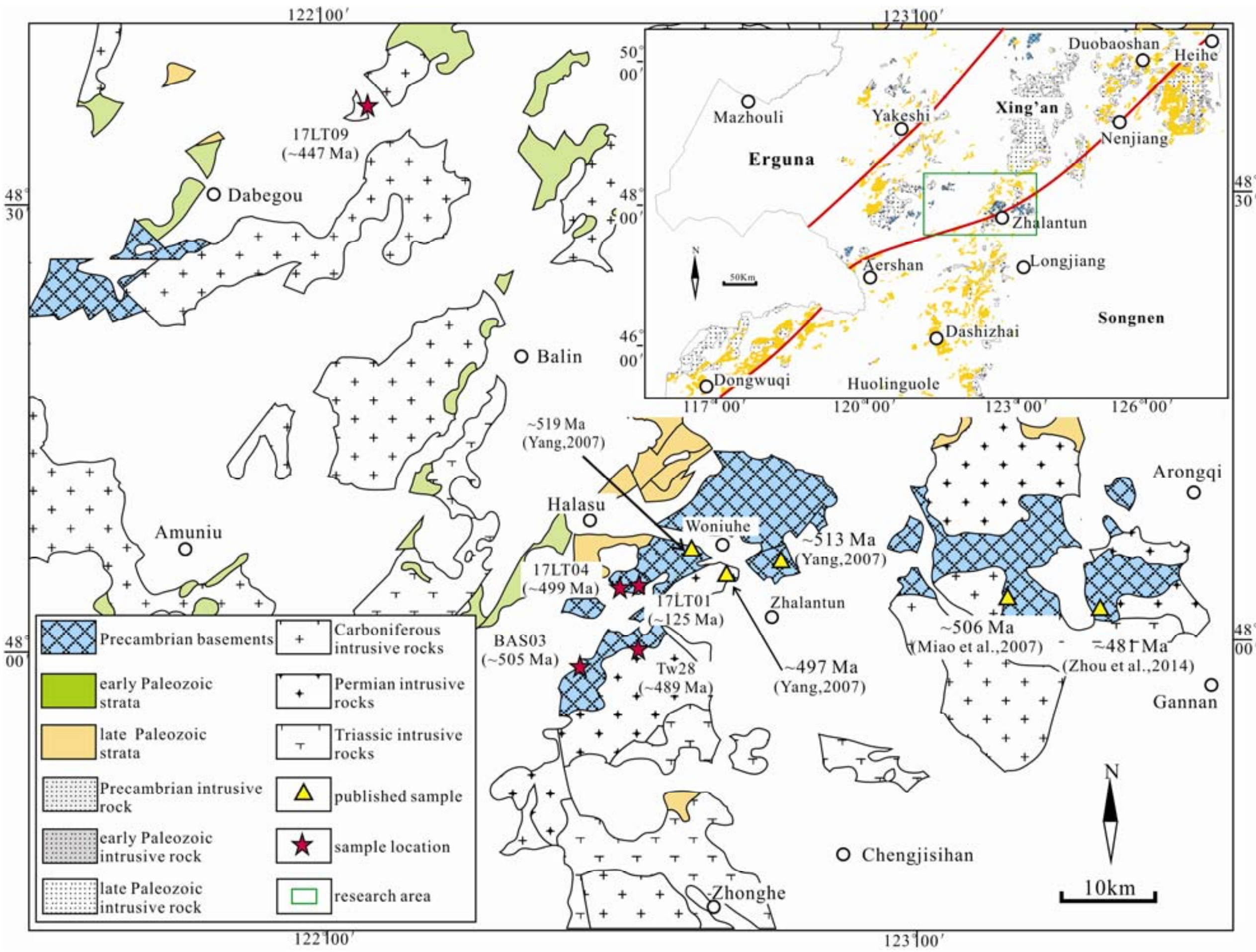

Fig. 1. Geological map of the Zhalantun, Xing'an Massif and sample locations (after 1:250 000 Zhalantun RGS). The right insert diagram is a regional tectonic map of NE China (after Yang Yajun (unpublished)).

Table 1 Locations and petrology for collected rocks from Zhalantun

Previous research result	Sample	Location	Lithology	Latitude	Longitude	Mineral assemblages
Supposed Proterozoic supracrustal rocks	BAS03-1	SW	Rhyolite	47°55'30"N	122°25'39"E	Phenocryst of Qz, matrix of Qz + feldspar +Amp
	BAS03-2			47°55'30"N	122°25'39"E	
	BAS03-3			47°55'30"N	122°25'39"E	
	BAS03-4			47°55'30"N	122°25'39"E	
	BAS03-5			47°55'30"N	122°25'39"E	
	17LT04-1	NW	Chloritization muscovite schist	48°04'25"N	122°30'50"E	Ms (~70%)+Chl (~9 - 12%)+ Pl-Qz (~15%)
	TW28	SW	Siltstone	47°58'34"N	122°31'45"E	clastic particles of Qz+Pl, matrix of Ms+Bi
Supposed Proterozoic plutons	17LT09-1	Yalu, NE Dabeigou	Amphibole gabbro	48°36'32"N	122°03'46"E	Pl(~40–58%)+Amp (~30-45%)+Mt (~5–10%)±Cpx+Epi+Chl+Tnt
	17LT09-2			48°36'32"N	122°03'46"E	
	17LT09-3			48°36'32"N	122°03'46"E	
	17LT09-5			48°36'32"N	122°03'46"E	
	17LT09-6			48°36'32"N	122°03'46"E	
	17LT01-6	Lingxi, NE Zhalantun	Quartz diorite	48°04'26"N	122°31'00"E	Pl (~35%)+Kfs (~22%)+Qz (~14%) +Bi-Amp-Cpx (~25%)+Ap+Zrn

Abbreviations: Qz-quartz; Pl-plagioclase; Kfs- K- feldspar; Amp- amphibole; Ms-muscovite; Chl-chlorite; Bi-biotite; Mt-magnetite; Cpx-clinopyroxene; Epi-epidote; Zrn-zircon.

epidote and chlorite. Zircons locally occur as accessory minerals. Chloritization muscovite schist (17LT04-1) was intruded by later quartz veins. Muscovite schist exhibits scaly blastic texture and schistose structure, and is composed of muscovite (~70%), plagioclase + quartz (~15%), chlorite (~9–12%), and accessory minerals of epidote and black opaque minerals (Fig. 2c and d). Siltstone (TW28) from the southwestern Zhalantun area

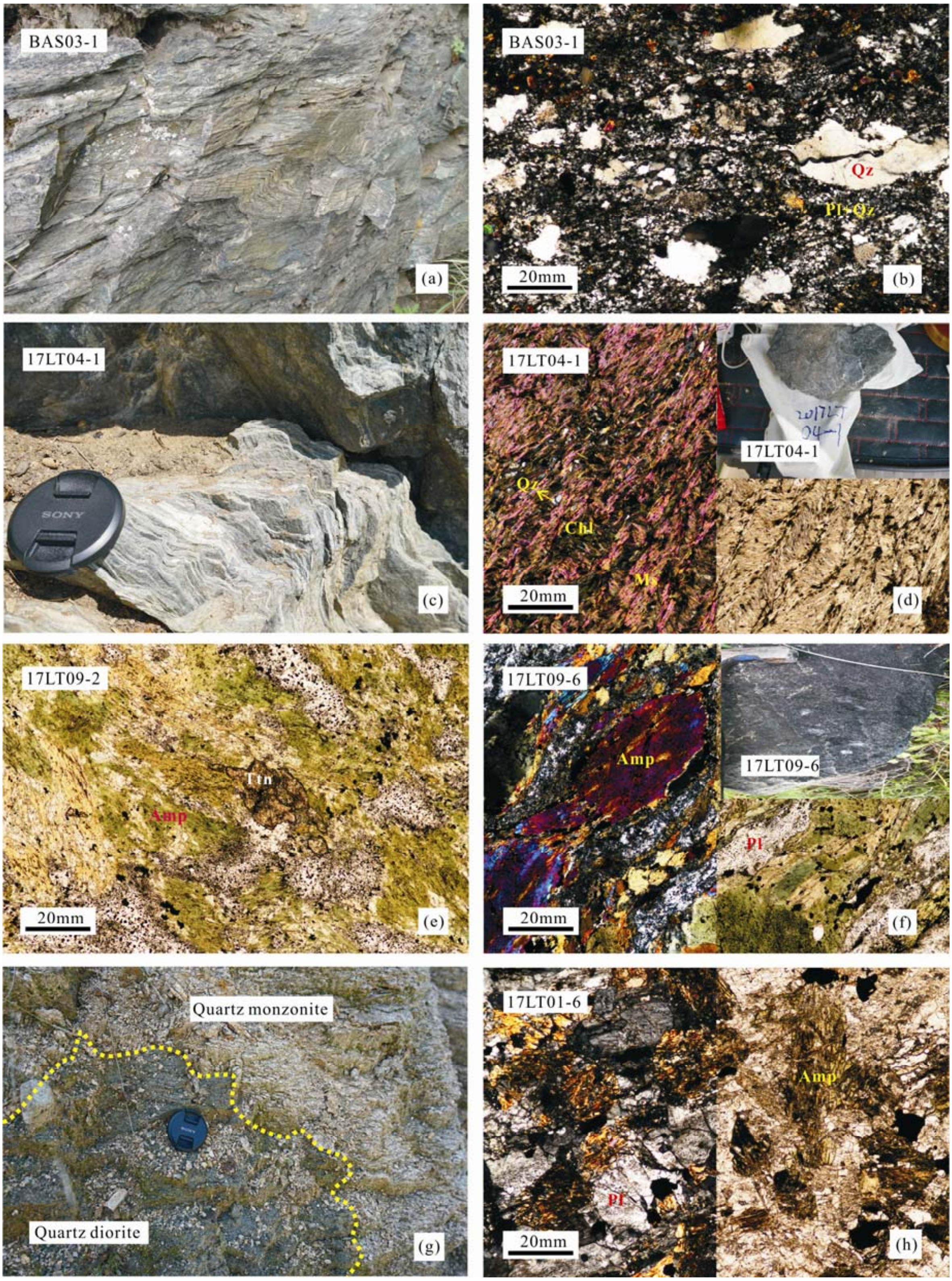

Fig. 2. Outcrop photograph (a) and photomicrograph (b) for rhyolite (BAS03-1); outcrop photograph (c) and photomicrograph (d) for muscovite schist (17LT04-1). The right insert image within Figure d is a hand specimen of the sample 17LT04-1. Photomicrographs for amphibole gabbros 17LT09-2 (e) and 17LT09-6 (f). The right insert image within Figure f is a hand specimen of sample 17LT09-6. (g) The quartz diorite was occurred as a xenolith within the quartz monzonite. (h) Photomicrograph for quartz diorite 17LT01-6. The left and right images in the D, F and H were captured under perpendicular polarized light and plane polarized light, respectively.

Abbreviations: Amp: amphibole; Pl: plagioclase; Qz: quartz; Ms: muscovite; Ttn: titanite; Chl: chlorite.

yields clastic texture and schistose structure. Clastic particles of siltstone are mainly quartz and plagioclase, and matrix are dominated by muscovite and minor biotite.

Amphibole gabbros outcrop in the Yalu area, northeast of Dabeigou, and is locally intruded by felsic veins. Five (chloritization) amphibole gabbros (samples 17LT09-1, 17LT09-2, 17LT09-3, 17LT09-5 and 17LT09-6) exhibit medium- to fine-grained textrues and massive to gneissic structures. These amphibole gabbros are dominated by plagioclase (~40–58%), amphibole+clinopyroxene (~30–45%) and black opaque minerals (~5–10%), accompanied with accessory minerals of epidote, chlorite, apatite and titanite (Fig. 2e and f). Clinopyroxene is locally preserved and surrounded by amphibole and opaque minerals (probably be magnetite), corresponding to a metamorphic reaction of Cpx+Pl+H_2O → Amp+Pl+Mt. These gabbros in the study area underwent low amphibole facies metamorphism. It is worth noting that samples 17LT09-1, 17LT09-2 and 17LT09-3 comprise much more titanite contents than the remained two amphibole gabbros (Fig. 2e).

The ~1048 Ma diorite outcrops in the Lingxi area, northwestern Zhalantun, and is actually re-defined as quartz diorite according to mineral assemblages. The 1:250 000 Zhalantun RGS reported that such diorite intruded the Xinghuadukou Group and therefore speculated that the Xinghuadukou Group formed before ~1048 Ma (He et al., 2006). However, no contact relationships between diorite and the Xinghuadukou Group were recognized. Locally quartz diorites expose as xenoliths within quartz monzonite with lengths of 0.5–1.5 meters (Fig. 2g). Quartz diorite (sample 17LT01-6) yields fine-grained texture and minerals of plagioclase (~35%), K-feldspar (~22%), quartz (~14%), Amphibole + Biotite + Clinopyroxene (~25%), accompanied with accessory minerals of apatite, zircon and opaque minerals (Fig. 2h).

3.2 Analytical methods

Rhyolites and amphibole gabbros were analyzed for whole-rock geochemical compositions at the Institute of Crustal Dynamics, China Earthquake Administration, which were pulverized to about 200-mesh size by an agate mill. Major oxides were determined by automatic X-ray fluorescence (XRF) spectrometry. The precision is 0.5% for major elements. Pre-treatment of trace element was finished using HF and HNO_3 mixture in Teflon bombs. Trace elements including rare earth elements (REE) were measured by a Thermo X-Series inductively-coupled plasma mass spectrometer (ICP-MS) after the HF and HNO_3 digestion of about 25 mg whole-rock powder in Teflon beakers. The GSR-1 (granite), GSR-3 (basalt) and GSR-15 (plagioclase amphibolite) were used as international reference to estimate the accuracies. The precision was better than 0.5% for trace element compositions. More detailed procedures were recorded by Liu et al. (2018, 2017, 2015, 2012, 2011a, b) and Guo et al. (2017a, b, 2015, 2013).

Zircon U-Pb dating was analyzed by laser ablation inductively coupled plasma mass spectrometry (LA-ICPMS) at the Laboratory of Ocean Lithosphere and Mantle Dynamics in Institute of Oceanology, Chinese Academy of Sciences. During the U-Th-Pb analyses, the multiple reference materials, e.g. NIST 610, USGS BCR-2G, were used to optimize the machine. Zircon 91500 (~1063 Ma), GJ-1 (~600 Ma) and Plešovice (~337 Ma) were used as the standard. ^{29}Si was applied as the internal standard for data calibration. The analytical precision is within 5%. Detailed descriptions for zircon U-Pb analytical processes were reported by Guo et al. (2018, 2017a, b). The ^{207}Pb/^{206}Pb, ^{206}Pb/^{238}U, ^{207}Pb/^{235}U and ^{208}Pb/^{232}Th ratios and apparent ages were calculated by Glitter 4.4 (van Achterbergh et al., 2001). Age calculations and concordia diagrams were performed by ISOPLOT 3.0 (Ludwig, 2003).

Zircon in-situ Lu-Hf isotopes were analyzed by a NU plasma II MC-ICPMS at the School of Earth and Space Science, Peking University. An ArF excimer laser ablation system of Geolas HD (193 nm) was applied with 40 μm spotsize. Zircon 91500, Plešovice and Penglai were used as internal standard and yield ^{176}Hf/^{177}Hf values of 0.282306±0.000020, 0.282457±0.000011 and 0.282895±0.000019 during the experiment, respectively, which are within the error of reported values (Wu et al., 2007). The analytical procedure was descripted by Zhang et al. (2016) in detail.

4 Analytical Results

4.1 Zircon U-Pb dating results

4.1.1 Ages of the supposed Proterozoic supracrustal rocks

Muscovite schist, rhyolite and siltstone were collected from the Proterozoic Xinghuadukou Group and Jiageda Formation and were analyzed for zircon U-Pb isotopes, among which rhyolite was chosen to analyze for zircon Lu-Hf isotopes. The detailed results are listed in Table 2.

A total of twenty spots were analyzed on twenty zircon grains from the rhyolite BAS03-3 that nearly all exhibited prismatic shapes and clear oscillatory zones (Fig. 3a), with lengths of 60–180 μm and length/width ratios of 2:1–4:1. Together with high Th/U ratios of 1.13–0.14 (except spot #17 with low Th/U ratio of 0.06), almost analyzed zircons yield magmatic characteristics (e.g., Yang et al., 2014; Zeng et al., 2017). Apparent ^{206}Pb/^{238}U ages of rhyolite are widely distributed from 500±9 Ma to 2865±35 Ma (apparent ^{207}Pb/^{206}Pb ages are used in this paper when they are >1000 Ma). The youngest age group is constructed by eleven analyses whose apparent ^{206}Pb/^{238}U ages are from 500±9 Ma to 516±12 Ma, and falls on the concordia curve (Fig. 4a) with a weighted mean ^{206}Pb/^{238}U age of 505±5 Ma (MSWD=0.18). Seven analyses (spot #2, #6, #9, #10, #14, #16 and #20) give apparent ^{206}Pb/^{238}U ages of 920±19 Ma – 929±14 Ma and fall on the concordia curve (Fig. 4a). The remained two analyses #15 and #17 yield the oldest apparent ^{207}Pb/^{206}Pb ages of 2865±35 Ma and 2594±43 Ma, respectively. Taken together, the youngest weighted mean ^{206}Pb/^{238}U age of 505±5 Ma (n=11) represents the formation age of rhyolite, while the older ages of ~920 – 929 Ma, ~2594 Ma and ~2865 Ma could be ages of the xenocryst zircons.

Muscovite schist 17LT04-1 was collected in the Luodiyingzi of Zhalantun city. A total of forty U-Th-Pb

Table 2 Zircon U-Pb isotopic data for collected samples from the Zhalantun basements

Sample No.	Th/U	$^{207}Pb/^{206}Pb$		$^{207}Pb/^{235}U$		$^{206}Pb/^{238}U$		$^{207}Pb/^{206}Pb$		$^{207}Pb/^{235}U$		$^{206}Pb/^{238}U$	
	ratios	Ratio	1σ	Ratio	1σ	Ratio	1σ	Ag(Ma)	1σ	Ag(Ma)	1σ	Age(Ma)	1σ
BAS03-3													
BAS03-3-1	0.50	0.0497	0.0013	0.5777	0.0200	0.0833	0.0019	189	61	463	13	516	12
BAS03-3-2	0.24	0.0640	0.0020	1.3695	0.0483	0.1534	0.0035	743	65	876	21	920	19
BAS03-3-3	0.34	0.0511	0.0017	0.5807	0.0218	0.0816	0.0021	243	78	465	14	506	13
BAS03-3-4	0.31	0.0536	0.0015	0.6008	0.0169	0.0807	0.0015	354	65	478	11	500	9
BAS03-3-5	0.24	0.0539	0.0017	0.6045	0.0168	0.0810	0.0014	365	70	480	11	502	9
BAS03-3-6	0.26	0.0688	0.0016	1.4849	0.0373	0.1550	0.0025	894	44	924	15	929	14
BAS03-3-7	0.25	0.0569	0.0011	0.6412	0.0149	0.0811	0.0014	487	44	503	9	503	8
BAS03-3-8	1.13	0.0566	0.0013	0.6376	0.0155	0.0814	0.0014	476	45	501	10	504	8
BAS03-3-9	1.07	0.0672	0.0024	1.4105	0.0452	0.1533	0.0027	843	74	893	19	920	15
BAS03-3-10	0.14	0.0694	0.0016	1.4788	0.0381	0.1539	0.0027	922	49	922	16	923	15
BAS03-3-11	0.50	0.0609	0.0019	0.6850	0.0202	0.0823	0.0014	635	67	530	12	510	8
BAS03-3-12	0.22	0.0586	0.0012	0.6620	0.0154	0.0819	0.0015	554	46	516	9	507	9
BAS03-3-13	0.60	0.0563	0.0012	0.6374	0.0154	0.0817	0.0013	465	53	501	10	506	8
BAS03-3-14	0.53	0.0655	0.0013	1.3900	0.0275	0.1535	0.0024	791	41	885	12	920	13
BAS03-3-15	0.61	0.2047	0.0044	16.034	0.3748	0.5683	0.0124	2865	35	2879	22	2901	51
BAS03-3-16	0.14	0.0698	0.0022	1.4863	0.0462	0.1538	0.0039	922	66	925	19	922	22
BAS03-3-17	0.06	0.1736	0.0044	12.823	0.3879	0.5350	0.0180	2594	43	2667	29	2762	75
BAS03-3-18	0.49	0.0572	0.0018	0.6458	0.0195	0.0820	0.0017	502	69	506	12	508	10
BAS03-3-19	0.23	0.0583	0.0015	0.6618	0.0199	0.0814	0.0015	543	57	516	12	504	9
BAS03-3-20	0.31	0.0724	0.0015	1.5527	0.0331	0.1545	0.0025	998	36	952	13	926	14
17LT04-1													
17LT04-1-1	0.70	0.0564	0.0013	0.6418	0.0158	0.0812	0.0014	567	51	496	9	482	8
17LT04-1-2	0.24	0.1161	0.0024	5.4529	0.1226	0.3362	0.0059	483	56	502	10	505	9
17LT04-1-3	0.72	0.0577	0.0013	0.6547	0.0166	0.0808	0.0013	600	60	537	12	542	11
17LT04-1-4	0.74	0.0583	0.0016	0.6462	0.0179	0.0799	0.0014	1898	42	1893	19	1868	29
17LT04-1-5	0.38	0.0587	0.0014	0.6609	0.0156	0.0816	0.0016	2117	28	2079	18	2024	27
17LT04-1-6	0.64	0.0591	0.0013	0.6649	0.0179	0.0809	0.0016	2362	31	2210	20	2044	32
17LT04-1-7	0.58	0.0568	0.0014	0.6393	0.0168	0.0815	0.0015	2224	41	2202	29	2140	41
17LT04-1-8	0.65	0.0561	0.0012	0.6354	0.0154	0.0817	0.0014	2440	31	2421	19	2387	32
17LT04-1-9	0.18	0.0696	0.0013	1.5324	0.0331	0.1584	0.0028	2399	35	2416	22	2416	40
17LT04-1-10	0.46	0.0706	0.0019	1.4496	0.0429	0.1473	0.0029	576	74	498	13	485	10
17LT04-1-11	0.06	0.1397	0.0033	7.7438	0.2496	0.3937	0.0089	413	41	486	8	495	8
17LT04-1-12	1.02	0.1115	0.0028	5.2102	0.1456	0.3369	0.0069	554	51	507	10	495	10
17LT04-1-13	0.67	0.0601	0.0019	0.6665	0.0217	0.0806	0.0019	543	64	506	11	496	8
17LT04-1-14	0.69	0.0593	0.0020	0.6332	0.0209	0.0781	0.0016	609	69	519	13	499	11
17LT04-1-15	0.61	0.0689	0.0016	1.3567	0.0343	0.1412	0.0026	520	44	511	10	501	8
17LT04-1-16	0.49	0.0590	0.0016	0.7129	0.0191	0.0877	0.0017	572	50	518	11	501	9
17LT04-1-17	0.67	0.0587	0.0021	0.7283	0.0382	0.0877	0.0018	546	63	512	12	503	9
17LT04-1-18	0.47	0.0691	0.0013	1.4860	0.0304	0.1548	0.0028	478	50	503	10	503	8
17LT04-1-19	0.54	0.0592	0.0015	0.6750	0.0184	0.0822	0.0016	494	50	504	10	505	9
17LT04-1-20	0.67	0.0548	0.0016	0.6299	0.0182	0.0826	0.0015	567	50	515	10	506	9
17LT04-1-21	0.26	0.1048	0.0022	4.6784	0.1146	0.3205	0.0065	454	48	499	10	506	9
17LT04-1-22	0.52	0.0557	0.0014	0.6684	0.0162	0.0867	0.0017	576	57	524	11	509	10
17LT04-1-23	0.29	0.0684	0.0012	1.5066	0.0338	0.1574	0.0028	406	69	496	11	512	9
17LT04-1-24	0.66	0.0551	0.0010	0.6136	0.0134	0.0798	0.0013	520	46	523	9	524	9
17LT04-1-25	0.91	0.1547	0.0031	9.7965	0.2361	0.4547	0.0089	476	44	518	9	526	8
17LT04-1-26	0.52	0.0992	0.0022	3.9203	0.0995	0.2842	0.0055	543	45	533	11	529	9
17LT04-1-27	0.67	0.0571	0.0013	0.6419	0.0162	0.0814	0.0015	443	54	520	10	536	10
17LT04-1-28	0.41	0.0581	0.0018	0.6964	0.0201	0.0878	0.0018	567	76	556	22	542	11
17LT04-1-29	0.34	0.1586	0.0030	9.8482	0.2012	0.4482	0.0072	565	64	546	11	542	10
17LT04-1-30	0.36	0.1058	0.0023	4.4448	0.1123	0.3040	0.0060	787	47	792	16	787	14
17LT04-1-31	0.13	0.0583	0.0013	0.6909	0.0176	0.0855	0.0016	898	46	870	15	852	15
17LT04-1-32	0.15	0.1514	0.0028	7.8186	0.1727	0.3731	0.0069	946	50	910	18	886	16
17LT04-1-33	0.96	0.0654	0.0016	1.1805	0.0344	0.1298	0.0024	902	38	925	12	928	15
17LT04-1-34	0.35	0.0566	0.0011	0.6661	0.0140	0.0851	0.0014	883	31	933	14	943	16
17LT04-1-35	1.18	0.0577	0.0019	0.6165	0.0212	0.0776	0.0017	517	66	488	13	482	10
17LT04-1-36	0.84	0.0587	0.0013	0.6298	0.0144	0.0777	0.0014	917	38	943	13	948	16
17LT04-1-37	0.18	0.0577	0.0012	0.6734	0.0152	0.0846	0.0016	1610	41	1618	21	1612	28
17LT04-1-38	0.58	0.1313	0.0022	6.7477	0.1343	0.3689	0.0058	1728	39	1721	21	1711	30
17LT04-1-39	0.56	0.0585	0.0017	0.6555	0.0199	0.0811	0.0016	1722	39	1763	21	1792	32
17LT04-1-40	0.65	0.0587	0.0012	0.6482	0.0156	0.0798	0.0016	1825	41	1854	24	1872	33
TW28													
TW28-1	0.80	0.1563	0.0032	8.5274	0.2112	0.4255	0.0074	2416	34	2289	23	2285	34
TW28-2	0.34	0.0589	0.0013	0.7040	0.0159	0.0876	0.0015	563	47	541	9	542	9
TW28-3	0.10	0.1891	0.0038	12.5534	0.2486	0.5102	0.0089	2734	33	2647	19	2658	38
TW28-4	0.62	0.1822	0.0037	12.5981	0.2489	0.5080	0.0088	2673	33	2650	19	2648	38
TW28-5	0.50	0.0630	0.0018	0.7301	0.0259	0.0897	0.0017	707	59	557	15	554	10
TW28-6	1.35	0.0584	0.0012	0.7021	0.0131	0.0881	0.0015	544	44	540	8	545	9
TW28-7	0.45	0.0588	0.0013	0.7085	0.0151	0.0877	0.0015	559	46	544	9	542	9

Continued Table 2

Sample No.	Th/U	$^{207}Pb/^{206}Pb$		$^{207}Pb/^{235}U$		$^{206}Pb/^{238}U$		$^{207}Pb/^{206}Pb$		$^{207}Pb/^{235}U$		$^{206}Pb/^{238}U$	
	ratios	Ratio	1σ	Ratio	1σ	Ratio	1σ	Age(Ma)	1σ	Age(Ma)	1σ	Age(Ma)	1σ
TW28-8	0.79	0.0567	0.0012	0.6145	0.0131	0.0783	0.0014	480	47	486	8	486	8
TW28-9	0.55	0.0604	0.0015	0.7052	0.0206	0.0865	0.0016	619	54	542	12	535	9
TW28-10	0.94	0.0640	0.0026	0.9178	0.0554	0.1079	0.0023	742	83	661	29	660	13
TW28-11	0.84	0.0550	0.0013	0.6170	0.0165	0.0790	0.0014	413	53	488	10	490	8
TW28-12	0.66	0.0592	0.0012	0.7055	0.0142	0.0880	0.0015	575	45	542	8	543	9
TW28-13	0.49	0.0583	0.0013	0.6092	0.0139	0.0781	0.0014	539	49	483	9	485	8
TW28-14	0.50	0.0594	0.0012	0.7109	0.0142	0.0878	0.0015	580	45	545	8	543	9
TW28-15	0.59	0.0586	0.0013	0.7100	0.0150	0.0882	0.0016	554	46	545	9	545	9
TW28-16	1.50	0.0639	0.0018	0.9193	0.0337	0.1080	0.0020	739	58	662	18	661	12
TW28-17	0.99	0.0696	0.0018	1.0739	0.0369	0.1216	0.0023	916	53	741	18	740	13
TW28-18	0.86	0.0682	0.0015	1.0734	0.0246	0.1222	0.0022	873	44	740	12	743	12
TW28-19	0.43	0.0611	0.0013	0.7104	0.0151	0.0879	0.0016	642	45	545	9	543	9
TW28-20	0.32	0.0592	0.0016	0.7076	0.0234	0.0882	0.0016	574	58	543	14	545	10
TW28-21	0.65	0.0654	0.0018	1.0494	0.0378	0.1189	0.0022	786	56	729	19	724	13
TW28-22	0.44	0.0723	0.0016	1.5926	0.0370	0.1620	0.0029	995	43	967	15	968	16
TW28-23	0.48	0.0587	0.0012	0.7074	0.0140	0.0878	0.0015	558	45	543	8	543	9
TW28-24	0.77	0.0649	0.0015	1.0808	0.0289	0.1222	0.0022	772	48	744	14	743	13
TW28-25	1.18	0.0580	0.0013	0.7052	0.0154	0.0875	0.0016	529	47	542	9	540	9
TW28-26	0.33	0.0572	0.0012	0.6239	0.0133	0.0794	0.0014	500	47	492	8	493	8
TW28-27	0.46	0.0571	0.0016	0.6213	0.0214	0.0786	0.0015	495	62	491	13	488	9
TW28-28	0.46	0.0580	0.0012	0.7069	0.0141	0.0878	0.0015	531	45	543	8	543	9
TW28-29	0.51	0.0566	0.0012	0.6265	0.0137	0.0795	0.0014	474	48	494	9	493	8
TW28-30	0.51	0.0682	0.0015	1.2711	0.0279	0.1377	0.0024	873	43	833	12	832	14
17LT09-3													
17LT09-3-01	0.26	0.0567	0.0014	0.5668	0.0160	0.0716	0.0014	480	90	456	10	446	8
17LT09-3-02	0.33	0.0561	0.0029	0.5432	0.0237	0.0714	0.0020	457	112	441	16	445	12
17LT09-3-03	0.50	0.0554	0.0012	0.5505	0.0123	0.0716	0.0011	428	50	445	8	446	7
17LT09-3-04	0.19	0.0596	0.0023	0.7302	0.0273	0.0878	0.0020	591	83	557	16	543	12
17LT09-3-05	0.30	0.0567	0.0015	0.5645	0.0168	0.0716	0.0014	480	61	454	11	446	9
17LT09-3-06	0.27	0.0575	0.0048	0.5619	0.0422	0.0715	0.0029	509	181	453	27	445	17
17LT09-3-07	0.34	0.0548	0.0026	0.5436	0.0255	0.0702	0.0016	406	107	441	17	437	10
17LT09-3-08	0.51	0.0633	0.0023	0.9990	0.0500	0.1130	0.0045	720	76	703	25	690	26
17LT09-3-09	0.16	0.0563	0.0027	0.5626	0.0343	0.0718	0.0034	461	106	453	22	447	20
17LT09-3-10	0.14	0.0587	0.0037	0.6500	0.0341	0.0822	0.0051	567	135	508	21	509	30
17LT09-3-11	0.25	0.0669	0.0040	0.7109	0.0449	0.0769	0.0033	835	131	545	27	477	20
17LT09-3-12	0.53	0.0557	0.0023	0.5652	0.0298	0.0736	0.0030	443	93	455	19	458	18
17LT09-3-13	0.38	0.0570	0.0015	0.5759	0.0164	0.0737	0.0016	500	56	462	11	459	10
17LT09-3-14	0.34	0.0608	0.0029	0.7960	0.0345	0.0951	0.0025	632	104	595	20	586	15
17LT09-3-15	0.97	0.0598	0.0054	0.5703	0.0505	0.0720	0.0053	594	203	458	33	448	32
17LT09-3-16	0.69	0.0737	0.0059	1.8584	0.2235	0.1785	0.0128	1035	164	1066	79	1059	70
17LT09-3-17	0.19	0.0594	0.0017	0.8337	0.0266	0.1011	0.0021	583	61	616	15	621	12
17LT09-3-18	0.22	0.0575	0.0017	0.5803	0.0168	0.0741	0.0020	509	65	465	11	461	12
17LT09-3-19	0.43	0.0634	0.0013	0.9372	0.0197	0.1076	0.0018	720	43	671	10	659	11
17LT09-3-20	0.44	0.0549	0.0046	0.5305	0.0414	0.0712	0.0031	406	187	432	27	443	19
17LT09-3-21	0.41	0.0566	0.0023	0.5436	0.0206	0.0712	0.0018	476	89	441	14	444	11
17LT09-3-22	0.39	0.0929	0.0091	1.2960	0.1901	0.0965	0.0041	1487	187	844	84	594	24
17LT09-3-23	0.29	0.0617	0.0023	0.8825	0.0346	0.1038	0.0035	665	80	642	19	637	21
17LT09-3-24	1.09	0.0567	0.0022	0.6210	0.0320	0.0784	0.0027	480	87	491	20	487	16
17LT09-3-25	0.41	0.0919	0.0130	0.9564	0.1480	0.0734	0.0038	1466	275	681	77	457	23
17LT09-3-26	0.38	0.0646	0.0033	0.6418	0.0384	0.0712	0.0026	761	105	503	24	443	15
17LT09-3-27	0.30	0.0571	0.0029	0.5601	0.0292	0.0723	0.0033	494	111	452	19	450	20
17LT09-3-28	0.39	0.0572	0.0015	0.5674	0.0163	0.0721	0.0016	498	62	456	11	449	9
17LT09-3-29	0.28	0.0771	0.0034	0.6892	0.0346	0.0654	0.0030	1124	87	532	21	409	18
17LT09-3-30	0.80	0.0577	0.0015	0.6179	0.0152	0.0779	0.0018	517	56	489	10	483	11
17LT01-6													
17LT01-6-1	0.68	0.0519	0.0047	0.1375	0.0122	0.0199	0.0012	283	211	131	11	127	7
17LT01-6-2	0.68	0.0497	0.0047	0.1319	0.0117	0.0199	0.0009	189	198	126	11	127	6
17LT01-6-3	0.76	0.0493	0.0033	0.1277	0.0080	0.0194	0.0006	161	161	122	7	124	4
17LT01-6-4	0.80	0.0493	0.0043	0.1368	0.0118	0.0204	0.0009	161	206	130	11	130	6
17LT01-6-5	1.72	0.1822	0.0113	0.4967	0.0300	0.0207	0.0006	2673	102	409	20	132	4
17LT01-6-6	0.99	0.0494	0.0029	0.1410	0.0090	0.0208	0.0008	169	134	134	8	133	5
17LT01-6-7	0.61	0.0517	0.0041	0.1348	0.0104	0.0192	0.0009	333	183	128	9	123	6
17LT01-6-8	0.70	0.0477	0.0043	0.1415	0.0131	0.0200	0.0008	87	200	134	12	128	5
17LT01-6-9	0.93	0.0510	0.0015	0.1335	0.0040	0.0190	0.0003	239	69	127	4	121	2
17LT01-6-10	0.86	0.0503	0.0029	0.1447	0.0083	0.0209	0.0005	209	131	137	7	133	3
17LT01-6-11	0.80	0.0492	0.0015	0.1323	0.0041	0.0196	0.0004	167	72	126	4	125	2
17LT01-6-12	0.64	0.0904	0.0133	0.2660	0.0284	0.0214	0.0012	1435	283	239	23	137	8
17LT01-6-13	2.09	0.1092	0.0049	0.2914	0.0117	0.0198	0.0004	1787	82	260	9	127	3
17LT01-6-14	0.64	0.0492	0.0027	0.1193	0.0068	0.0176	0.0005	167	125	114	6	112	3
17LT01-6-15	0.63	0.0478	0.0022	0.1303	0.0058	0.0194	0.0004	100	94	124	5	124	2

Continued Table 2

Sample No.	Th/U ratios	$^{207}Pb/^{206}Pb$		$^{207}Pb/^{235}U$		$^{206}Pb/^{238}U$		$^{207}Pb/^{206}Pb$		$^{207}Pb/^{235}U$		$^{206}Pb/^{238}U$	
		Ratio	1σ	Ratio	1σ	Ratio	1σ	Age(Ma)	1σ	Age(Ma)	1σ	Age(Ma)	1σ
17LT01-6-16	0.91	0.0492	0.0019	0.1322	0.0050	0.0195	0.0004	167	95	126	5	126	2
17LT01-6-17	0.60	0.0488	0.0033	0.1343	0.0087	0.0195	0.0006	139	161	128	8	125	4
17LT01-6-18	0.65	0.0485	0.0021	0.1310	0.0059	0.0193	0.0004	124	106	125	5	123	3
17LT01-6-19	0.80	0.0509	0.0022	0.1325	0.0052	0.0190	0.0004	235	66	126	5	121	2
17LT01-6-20	0.66	0.0595	0.0062	0.1599	0.0137	0.0201	0.0010	587	228	151	12	129	6
17LT01-6-21	0.71	0.0509	0.0031	0.1416	0.0083	0.0197	0.0006	239	136	134	7	126	4
17LT01-6-22	0.59	0.0501	0.0019	0.1548	0.0056	0.0229	0.0005	198	87	146	5	146	3
17LT01-6-23	0.62	0.0479	0.0021	0.1301	0.0062	0.0196	0.0005	95	100	124	6	125	3
17LT01-6-24	1.82	0.0494	0.0030	0.1416	0.0124	0.0204	0.0008	165	143	134	11	130	5
17LT01-6-25	3.89	0.0490	0.0013	0.1316	0.0041	0.0193	0.0004	146	63	126	4	123	3
17LT01-6-26	1.05	0.0492	0.0027	0.1360	0.0081	0.0202	0.0010	167	125	130	7	129	6
17LT01-6-27	0.29	0.0540	0.0014	0.1711	0.0050	0.0228	0.0005	372	60	160	4	145	3
17LT01-6-28	1.87	0.0501	0.0011	0.1361	0.0034	0.0195	0.0003	198	52	130	3	125	2
17LT01-6-29	1.63	0.0576	0.0021	0.1583	0.0060	0.0198	0.0005	517	82	149	5	126	3
17LT01-6-30	0.81	0.0512	0.0030	0.1368	0.0091	0.0197	0.0013	250	140	130	8	126	8

Fig. 3. Cathodoluminescence images of representative zircon grains from samples BAS03-3 (a), 17LT04-1 (b), TW28 (c), 17LT09-3 (d) and 17LT01-6 (e), which show the inner structures and analyzed locations.

spots were analyzed on forty zircon grains that exhibit long prismatic and oval shapes, with lengths of 50–150 μm and length/width ratios of 1:1–4:1. On cathodoluminescence images (Fig. 3b), most analyzed zircon grains exhibit clear oscillatory zones while some have banded structure (e.g., spot #13) or structureless zones (spot #8 and #25). Except spot #11 with low Th/U ratio of 0.06, the remained thirty-nine spots have relatively high Th/U ratios of 1.18–0.13 (mean Th/U ratio of 0.55). Combined with the inner structure and high Th/U ratios, most zircons are considered as magmatic origins (e.g., Yang et al., 2014; Zeng et al., 2017). Forty analyzed spots define a wide range of apparent $^{206}Pb/^{238}U$ ages from 482±10 Ma to 2440±31 Ma and plot on or close to the

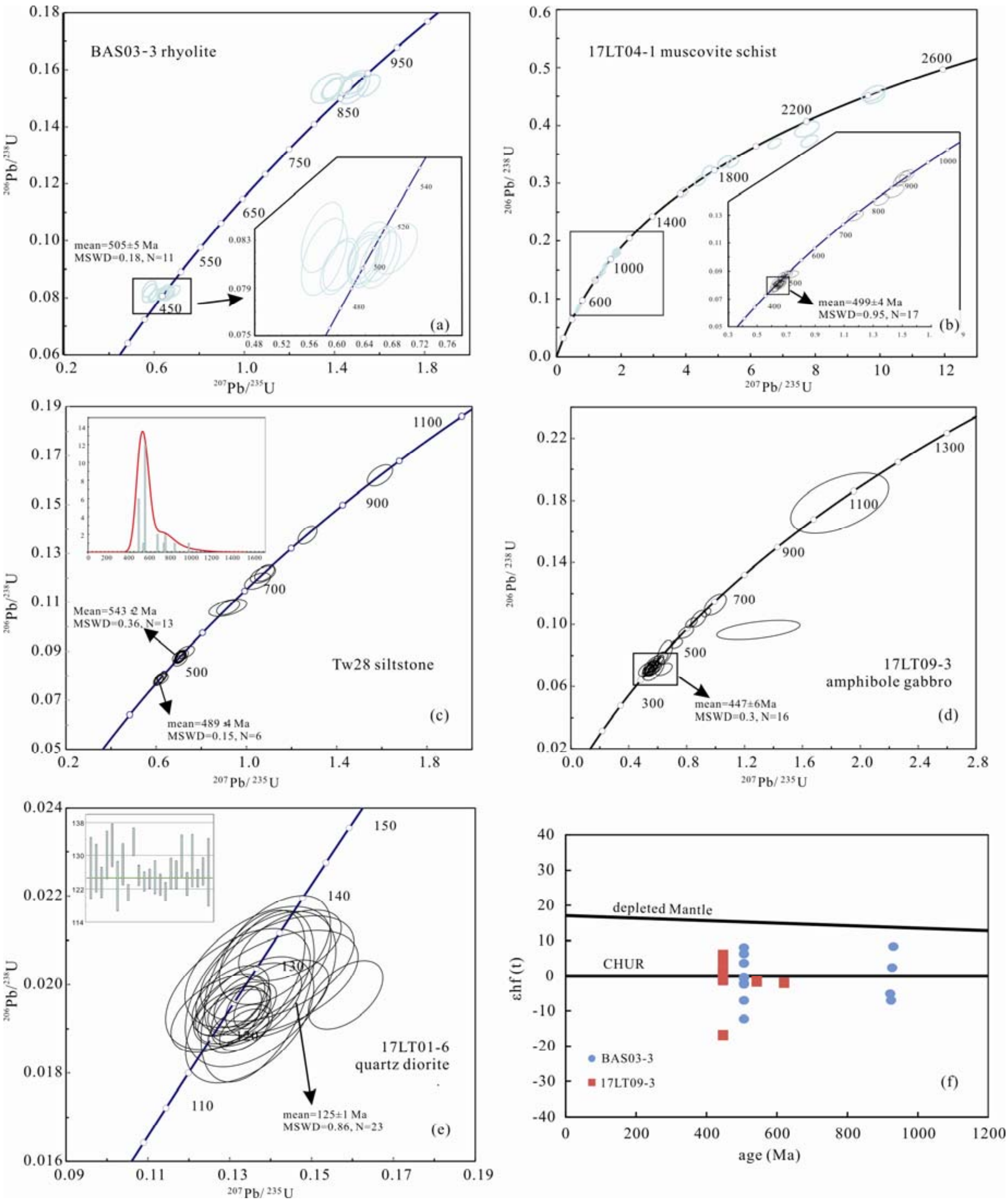

Fig. 4. U-Pb concordia diagrams for rhyolite BAS03-3 (a), muscovite schist 17LT04-1 (b), siltstone TW28 (c), amphibole gabbro 17LT09-3 (d) and quartz diorite 17LT01-6 (e). (f) Zircon *ε*Hf (*t*) values versus age (Ma) diagrams.

In Fig. 4 (f), rhyolite BAS03-3 (corrected to 505 Ma, except for the xenocryst zircons, which were corrected to their apparent $^{206}Pb/^{238}U$ ages): blue filled circle; Amphibole gabbro 17LT09-3 (corrected to 447 Ma, except for the xenocryst zircons, which were corrected to their apparent $^{206}Pb/^{238}U$ ages): red filled square; The $^{176}Lu/^{177}Hf$ values of the depleted mantle and chondrite are 0.0384 and 0.0332, respectively (Wu et al., 2007).

concordia curve on the U-Pb concordia diagram (Fig. 4b). According to apparent $^{206}Pb/^{238}U$ ages, all forty analyses can be divided into six age groups: (i) 482±10 Ma to 512±9 Ma (n=17), which yield the youngest weighted mean $^{206}Pb/^{238}U$ age of 499±4 Ma (MSWD=0.95); (ii) 524±9 Ma to 542±11 Ma (n=7); (iii) 787±14 Ma to–886±16 Ma (n=3); (iv) 928±15 Ma to 948±16 Ma (n=3); (v) apparent $^{207}Pb/^{206}Pb$ ages of 1610±41 Ma – 1898±42 Ma (n=5), and (vi) 2117±28 Ma to 2440±31 Ma (n=5). Yang (2007) interpreted chlorite/quartz schist in the Zhalantun area as metamorphic sedimentary rock based on petrological and geochemical characteristics. Therefore, the youngest weighted mean $^{206}Pb/^{238}U$ age of 499±4 Ma (n=17) represents the maximum depositional time of muscovite schist. Additionally, the older ages of ~787 Ma to 2440 Ma imply that Neoproterozoic – Paleoproterozoic detrital zircons were recorded in the Zhalantun.

A total of thirty analyses were conducted on thirty zircons from the siltstone TW28 with lengths of 80–200 μm and length/width ratios of 2:1–4:1. Most analyzed zircons exhibit clear oscillatory zones while some yield banded or structureless zones (Fig. 3c). Th/U ratios are 0.1 –1.5 with an average ratio of 0.65. Analyses of siltstone fall on the concordia curve (Fig. 4c) and yield a wide range of apparent $^{206}Pb/^{238}U$ ages of 485±8 Ma to 2734±33 Ma that can be divided into four age groups. The youngest age peak is dominated by six analyses and give apparent $^{206}Pb/^{238}U$ ages of 485±8 Ma to 493±8 Ma with a weighted mean $^{206}Pb/^{238}U$ age of 489±4 Ma (MSWD=0.15). The second age group comprises thirteen analyses with apparent $^{206}Pb/^{238}U$ ages of 535±9 Ma to 554±10 Ma. Eight analyses construct the third age peak and define apparent $^{206}Pb/^{238}U$ ages of 660±13 Ma to 968±16 Ma. The remained three analyses yield apparent $^{207}Pb/^{206}Pb$ ages of 2734±33 Ma to 2416±34 Ma. Collectively, the youngest weighted mean $^{206}Pb/^{238}U$ age of 489±4 Ma limit the maximum depositional age, while the older ages of ~535–554 Ma, ~660 – 968 Ma and ~2416–2734 Ma record ages for detrital zircons captures during sedimentary process.

4.1.2 Ages of the supposed Proterozoic plutons

Amphibole gabbro and quartz diorite were interpreted to be generated at 2096±36 Ma and 1048±443 Ma, respectively, by using single zircon U-Pb dilution method, though less than ten analyses for each sample were obtained (He et al., 2006). In order to determine whether they are Proterozoic plutons or not, we collected amphibole gabbro and quartz diorite in this study for zircon in-situ U-Pb isotopic analyses. The detailed results are listed in Table 2.

With respect to amphibole gabbro 17LT09-3, a total of thirty analyses were performed on thirty zircon grains that are prismatic, spherical-oval and flake shapes with lengths of 50–150 μm and length/width ratios of 1:1–3:1. Cathodoluminescence images (Fig. 3d) exhibit almost all zircon grains have high luminescence rims. Zircons yield oscillatory zoning (e.g. spot #1 and #15), patchy or structureless (e.g. spot #23 and #24) inner cores. Combined with high Th/U ratios of 0.14–1.09 (average: 0.41), most zircons are considered as magmatic origins. Thirty analyzed zircons yield a wide range of apparent $^{206}Pb/^{238}U$ ages of 409±18 – 1059±70 Ma. Spot #11, #22, #25 and #29 plot below the concordia curve owing to Pb loss and are excluded from following age calculations (Fig. 4d), while the remained twenty-six fall on the U-Pb concordia curve. Sixteen analyses with apparent $^{206}Pb/^{238}U$ ages of 437±10 to 461±11 Ma construct the largest and youngest age group and define a weighted mean $^{206}Pb/^{238}U$ age of 447±6 Ma (MSWD=0.3), which is interpreted as the crystallization age of the amphibole gabbro. The remained ten analyses yield older apparent $^{206}Pb/^{238}U$ ages of 483±11 to 1059±70 Ma, indicative of ages for xenocryst zircon captured during magma ascent.

Quartz diorite 17LT01-6 outcrops in the Lingxi area. A total of thirty analyses were carried out on thirty zircon grains, which present long-prismatic, oval or flake shapes and lengths of 60–110 μm and length/width ratios of 1:1–3:1. On cathodoluminescence images (Fig. 3e), almost zircons exhibit clear oscillatory zoning structure while minor zircons yield structureless features (e.g. spot #25). Analyzed zircons have high Th/U ratios of 0.29–3.89 (average: 1.01). Analyses #14 was conducted on inclusions within a zircon, resulting in unstable signal during experiment, and was therefore excluded in the following age calculations. The remained twenty-nine analyses yield apparent $^{206}Pb/^{238}U$ ages from 112±3 to 146±3 Ma. On the U-Pb concordia diagram (Fig. 4e), except spot #5, #12, #13 and #20, the remained twenty-five analyses plot on the concordia curve (Fig. 4e), among which twenty-three analyses give apparent $^{206}Pb/^{238}U$ ages of 121±2 to 133±5 Ma and a weighted mean $^{206}Pb/^{238}U$ age of 125±1 Ma (MSWD=0.86), indicative of the magmatic age of quartz diorite. In addition, analyses #22 and #27 yield older ages of 146±3 Ma and 145±3 Ma, respectively, representing xenocryst zircon ages.

4.2 Zircon Lu-Hf isotopes for early Paleozoic rocks

A total of fifteen Lu-Hf isotopic analyses were conducted for rhyolite BAS03-3, among which analyzed spot #3 yields abnormal signal during experiment and therefore can be excluded in later calculations. Analyses #1, #7, #8 and #11 were carried on xenocryst zircons and give $^{176}Hf/^{177}Hf_i$ values of 0.282262, 0.281998, 0.282053 and 0.282429, εHf (t) values of +2.4, −7.0, −5.1 and +8.4, and T_{DM} (Hf) of ~1376 Ma, 1742 Ma, 1667 Ma and 1140 Ma, respectively, when corrected to their apparent $^{206}Pb/^{238}U$ ages of ~926 Ma, ~923 Ma, ~920 Ma and ~929 Ma, respectively. The remained ten analyses with apparent $^{206}Pb/^{238}U$ ages of 500±9 Ma to 516±12 Ma yield $^{176}Hf/^{177}Hf_i$ values of 0.282687–0.282112, εHf(t) values of +8.1 to −12.2 and T_{DM}(Hf) of ~790 to 1584 Ma, respectively, when corrected to their formation age of 505 Ma. The ten analyses plot across the CHUR line on the εHf(t) vs. age diagram (Fig. 4f).

For amphibole gabbro 17LT09-3, a total of fifteen zircon in-situ Lu-Hf analyses were performed, among which analyses #7 yields abnormal peaks during experiment procedure and is precluded during later Lu-Hf calculations. Analyses #2 and #8 were carried on xenocryst zircons and give $^{176}Hf/^{177}Hf_i$ values of 0.282443 and 0.282437, εHf(t) values of +0.3 and +1.8, and T_{DM}(Hf)

Table 3 Zircon Lu-Hf isotopic and calculated data for rhyolite and gabbro from the Zhalantun basements

Sample No.	ApparentAge (Ma)	Crystallization Age (Ma)	$^{176}Yb/^{177}Hf$	$^{176}Lu/^{177}Hf$	$^{176}Hf/^{177}Hf$	2σ	$^{176}Hf/^{177}Hf_i$	$\varepsilon_{Hf}(t)$	T_{DM} (Ma)	$f_{Lu/Hf}$
BAS03-3										
BAS03-3-01	926		0.03754	0.001287	0.282284	0.000049	0.282262	+2.4	1376	−0.96
BAS03-3-02	504	505	0.03755	0.001044	0.282408	0.000045	0.282398	−2.1	1194	−0.97
BAS03-3-04	506	505	0.04596	0.001460	0.282404	0.000051	0.282390	−2.4	1213	−0.96
BAS03-3-05	507	505	0.03132	0.001436	0.282701	0.000048	0.282687	+8.1	790	−0.96
BAS03-3-06	510	505	0.02848	0.000909	0.282645	0.000051	0.282636	+6.3	857	−0.97
BAS03-3-07	923		0.03447	0.001095	0.282017	0.000037	0.281998	−7.0	1742	−0.97
BAS03-3-08	920		0.0416	0.001189	0.282074	0.000049	0.282053	−5.1	1667	−0.96
BAS03-3-09	504	505	0.0442	0.001266	0.282573	0.000061	0.282561	+3.7	968	−0.96
BAS03-3-10	503	505	0.02852	0.000721	0.282119	0.000041	0.282112	−12.2	1584	−0.98
BAS03-3-11	929		0.03972	0.001204	0.28245	0.000044	0.282429	+8.4	1140	−0.96
BAS03-3-12	502	505	0.0692	0.002000	0.28258	0.000059	0.282561	+3.7	977	−0.94
BAS03-3-13	500	505	0.018556	0.000567	0.282266	0.000041	0.282261	−7.0	1375	−0.98
BAS03-3-14	506	505	0.03198	0.001098	0.28246	0.000048	0.282450	−0.3	1123	−0.97
BAS03-3-15	516	505	0.0894	0.003380	0.282428	0.000052	0.282396	−2.2	1243	−0.90
17LT09-3										
17LT09-3-01	446	447	0.03335	0.001176	0.28248	0.00013	0.282470	−0.8	1097	−0.96
17LT09-3-02	543		0.067	0.002313	0.282467	0.000043	0.282443	+0.3	1150	−0.93
17LT09-3-03	445	447	0.008256	0.000269	0.282508	0.000058	0.282506	+0.4	1032	−0.99
17LT09-3-04	437	447	0.01865	0.000731	0.28267	0.00013	0.282664	+6.0	818	−0.98
17LT09-3-05	459	447	0.01056	0.000422	0.282487	0.000071	0.282483	−0.4	1065	−0.99
17LT09-3-06	448	447	0.04457	0.001551	0.282032	0.000064	0.282019	−16.8	1742	−0.95
17LT09-3-08	621		0.005362	0.000192	0.282439	0.000069	0.282437	+1.8	1125	−0.99
17LT09-3-09	443	447	0.02063	0.000856	0.282481	0.000056	0.282474	−0.7	1086	−0.97
17LT09-3-10	444	447	0.00729	0.000281	0.282537	0.000093	0.282535	+1.4	993	−0.99
17LT09-3-11	487	447	0.06545	0.002255	0.282526	0.000087	0.282507	+0.5	1062	−0.93
17LT09-3-12	457	447	0.02731	0.001003	0.282627	0.000067	0.282619	+4.4	885	−0.97
17LT09-3-13	450	447	0.02766	0.000911	0.282467	0.000067	0.282459	−1.2	1107	−0.97
17LT09-3-14	449	447	0.01567	0.000499	0.282509	0.000064	0.282505	+0.4	1037	−0.98
17LT09-3-15	483	447	0.04134	0.001429	0.28254	0.000074	0.282528	+1.2	1019	−0.96

of 1150 Ma and 1125 Ma, respectively, when corrected to their apparent $^{206}Pb/^{238}U$ age of 543 Ma and 621 Ma, respectively. The remained twelve analyses with apparent $^{206}Pb/^{238}U$ ages of 437±10 to 487±16 Ma yield $^{176}Hf/^{177}Hf_i$ values of 0.282019–0.282664, εHf(t) values of +6.0 to −16.8 and T_{DM} (Hf) of 818 Ma–1742 Ma, when corrected to their formation age of 447 Ma. On the εHf(t) versus Age diagram (Fig. 4f), these analyses mainly plot between CHUR and depleted mantle lines while some plot below the CHUR lines.

4.3 Whole-rock major and trace element compositions

Rhyolites and amphibole gabbros that were previously documented as the Proterozoic products were collected for whole-rock major and trace element analyses. The detailed data are listed in Table 4.

4.3.1 Effects of alteration and regional metamorphism on element mobility

The Zhalantun basements underwent multi-magmatic activities and experienced a complicated and long tectonic evolutionary history, e.g. Paleo-Asian Ocean tectonic activities and magmatisms. The supposed Proterozoic Zhalantun basements underwent greenschist to amphibolite facies metamorphisms. Therefore, evaluating the element mobility is essential before employing these geochemical data for discussing petrogenesis and tectonic setting.

Al_2O_3, TiO_2, high strength field elements (HFSEs), REEs, Cr, Ni, Sc and V are generally considered as stable compositions during later alteration and up to high amphibolite facies metamorphism (Polat, 2009; Polat and Hofmann, 2003), while large ion lithophile elements (LILEs), like Na, K, Rb and Sr, can be more easily altered and therefore be mobile. Under high amphibolite facies metamorphism, it is possible that Th can be unstable as well (Polat and Hofmann, 2003).

According to Polat and Hofmann (2003), loss on ignition (LOI) and Ce_N/Ce_N* ratio are closely related to alteration and metamorphism. All rhyolites and amphibole gabbros exhibit low LOI values (<3 wt%) and Ce_N/Ce_N* ratios of 0.88–1.16, implying that rhyolites and amphibole gabbros were not significantly altered by later metamorphism and alteration. In addition, on the major and trace elements vs. the alteration insensitive element Zr diagrams (Fig. 5), Rb, Sr and K_2O of rhyolites display scatter, while La, Ce, Yb, Na_2O, Th and Nb broadly follow linear trends. Sr, Na_2O, La, Ce, Nb and Yb of amphibole gabbros exhibit well linear trends, while Rb and K_2O yield considerable scatter. Th of samples 17LT09-5 and 17LT09 -6 display abnormal plots, indicative of mobility of Th for these two samples.

Collectively, Al_2O_3, TiO_2, REEs (e.g. La, Ce, Yb) and most HFSEs (e.g. Nb) for all rhyolites and amphibole gabbros, and Na_2O and Sr for amphibole gabbros are immobile, which can be employed to determine classification, petrogenesis and tectonic setting.

4.3.2 Whole-rock geochemical compositions for rhyolites

Rhyolites (sample BAS03) exhibit high SiO_2 (67.4–72.0 wt%) and alkaline contents (Na_2O+K_2O=3.64–4.55 wt%), and low Fe_2O_{3T} (4.65–5.75 wt%), TiO_2 (0.58–0.70 wt%) and Al_2O_3 (10.8–12.1 wt%), with relatively high MgO (2.53–3.03 wt%) and Mg$^{\#}$ (55–56, calculated as 100Mg^{2+}/

Table 4 Analytical data of whole rock major (wt%) and trace (ppm) elements and related parameters

Sample	BAS03-1	BAS03-2	BAS03-3	BAS03-4	BAS03-5	17LT09-1	17LT09-2	17LT09-3	17LT09-5	17LT09-6
SiO_2 (wt%)	70.9	67.4	71.9	72	71.9	45.7	49	47.7	44.9	44.1
Al_2O_3	11.4	12.1	11.4	11	10.8	14.4	11.9	15	17	19
CaO	3.02	3.7	2.13	3.34	3.66	16	17	15	8	12
Fe_2O_{3T}	4.99	5.75	4.77	4.74	4.65	12	9.16	9.97	12.2	13.2
K_2O	2.11	2.3	2.17	1.47	1.28	0.29	0.27	0.29	0.34	0.26
Na_2O	2.38	2.21	2.38	2.37	2.36	0.87	1.21	1.41	1.56	1.72
MgO	2.61	3.03	2.63	2.54	2.53	8.19	9.91	8.16	8.72	8.54
MnO	0.07	0.08	0.06	0.07	0.07	0.26	0.24	0.22	0.23	0.21
P_2O_5	0.18	0.19	0.18	0.17	0.16	0.1	0.28	0.29	0.22	0.09
TiO_2	0.59	0.7	0.6	0.59	0.58	1.74	0.75	1.33	1.13	1.14
$Mg^{\#}$	55	55	56	56	56	61	72	66	62	60
LOI	1.91	2.63	2	1.9	2.12	0.85	0.59	0.84	0.66	0.95
Li (ppm)	29	38	28	22	21	11.4	11.8	7.24	7.3	18
Sc	11.6	12.7	10.6	10.4	9.98	27	20	27	32	56
Ti	3536	4196	3596	3536	3477	10430	4495	7972	6773	6833
K	17516	19093	18014	12203	10626	2407	2241	2407	2823	2158
P	785	829	785	742	698	436	1222	1266	960	393
V	87	92	81	82	79	458	176	252	293	436
Cr	128	123	141	140	130	48	87	56	75	84
Co	0	0	0	0	0	33	24	29	33	43
Ni	44	46	48	41	40	32	35	31	28	18
Cu	20	25	21	20	21	42	233	18	64	11
Zn	69	85	69	62	60	181	295	175	149	113
Ga	15	17	16	16	16	19	14	16	19	20
Rb	95	81	92	45	43	10.1	4.66	4.42	7.15	6.45
Sr	247	326	231	328	318	413	342	381	394	414
Y	29	33	26	28	27	20	27	34	24	21
Zr	231	284	232	264	236	36	47	35	25	17
Nb	11.3	13.6	11.8	11	11	4.3	4.43	5.41	1.75	1.48
Cs	6.43	2.85	5.66	1.74	1.87	1.17	0.93	1.13	1.31	0.47
Ba	442	576	471	499	476	30	29	41	51	44
La	42	44	38	42	41	5.58	10.4	8.45	3.33	2.1
Ce	71	76	65	73	69	19	35	32	13.2	8.36
Pr	9.09	9.98	8.5	9.22	8.96	3.02	5.43	5.32	2.49	1.61
Nd	35	39	33	36	35	14.8	27	28	14.5	9.51
Sm	6.48	7.27	6.05	6.59	6.1	3.62	6.28	6.95	4.24	2.99
Eu	1.24	1.34	1.22	1.18	1.14	1.06	1.44	1.93	1.33	1.23
Gd	5.54	6.19	5.21	5.52	5.18	3.94	6.37	7.49	4.79	3.62
Tb	0.91	1.04	0.84	0.9	0.84	0.59	0.92	1.13	0.76	0.62
Dy	5.15	5.95	4.77	5.08	4.77	3.85	5.61	6.95	4.89	4.06
Ho	0.98	1.16	0.92	0.97	0.94	0.75	1.04	1.32	0.95	0.81
Er	2.78	3.3	2.58	2.79	2.64	2.32	3.16	3.95	2.87	2.49
Tm	0.45	0.52	0.4	0.45	0.41	0.26	0.34	0.42	0.31	0.27
Yb	2.99	3.61	2.76	3.08	2.86	1.97	2.61	3.2	2.33	2.16
Lu	0.41	0.49	0.37	0.42	0.4	0.24	0.31	0.36	0.27	0.25
Ta	0.9	1.03	0.81	0.78	0.79	0.28	0.31	0.37	0.09	0.1
Hf	2.57	3.19	2.33	2.64	2.5	1.38	2.22	1.6	1.25	0.89
Pb	24	26	25	23	21	24	49	30	20	10.1
Th	11.1	14.6	12.5	16	13.6	0.89	2.08	1.25	0.18	0.03
U	2.94	3.98	2.68	3.24	2.9	0.35	0.44	0.52	0.06	0.02
$(Nb/La)_{PM}$	0.38	0.43	0.55	0.46	0.42	0.74	0.41	0.62	0.51	0.68
$(La/Sm)_N$	2.43	2.75	2.23	2.45	2.51	1	1.07	0.79	0.51	0.45
$(La/Yb)_N$	6.36	6.71	5.4	5.87	6.05	2.03	2.86	1.89	1.02	0.7
$Eu_N/Eu_N{}^*$	1.25	1.16	1.03	1.19	1.2	0.86	0.7	0.82	0.9	1.14
Nb/Th	1.02	0.93	0.94	0.68	0.81	4.83	2.13	4.33	9.72	49
Ba/Nb	39	42	40	45	43	6.89	6.51	7.54	29	30
Lu/Yb	0.14	0.14	0.13	0.14	0.14	0.12	0.12	0.11	0.12	0.12
Th/Ce	0.16	0.19	0.19	0.22	0.2	0.05	0.06	0.04	0.01	0
Th/U	3.78	3.67	4.66	4.97	4.69	2.54	4.73	2.4	3	1.5
Sr/Y	8.67	9.88	8.78	11.7	12	21	12.6	11.2	16	20

Notes: wt%, major and minor element oxids in weight percent; ppm, trace elements in parts per million; LOI, loss on ignition; subscript N, chondrite normalized value; subscript PM, primitive mantle normalized value; $Mg^{\#}$=100Mg/(Mg+Fe_{total}) in atomic ratio; $Eu_N/Eu_N{}^*$=Eu_N/SQRT($Sm_N \times Gd_N$).

(Mg^{2+}+$Fe^{2+}{}_{total}$)). On the Zr/TiO_2 versus Nb/Yb and SiO_2 versus Zr/TiO_2 classification diagrams (Fig. 6a–b), rhyolites fall into rhyolite and dacite areas. On the FeO_T-Na_2O+K_2O-MgO triangular diagram (Fig. 6c), rhyolites follow alkaline-rich trend and lack Fe-rich trend, indicative of their calc-alkaline characteristics. Considering that K might be mobile, FeO_T/MgO versus SiO_2 diagram is applied as well (Fig. 6d), on which rhyolites all plots into calc-alkaline areas as well. On the SiO_2 versus major oxides diagrams (Fig. 6e–f, not all shown), Al_2O_3, Fe_2O_{3T} and TiO_2 of rhyolites construct negative correlations with SiO_2, while Na_2O define a

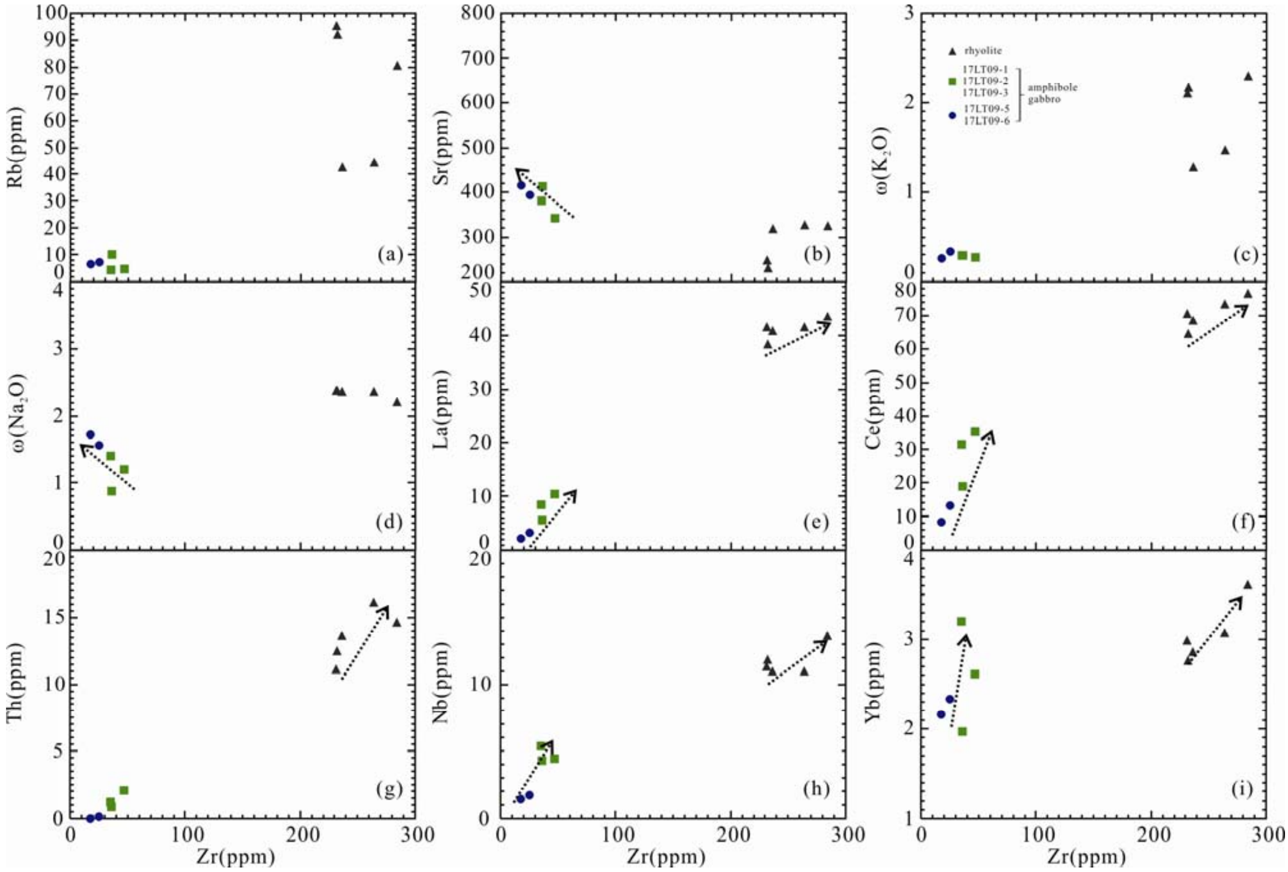

Fig. 5. Covariation diagrams of alteration insensitive element Zr versus Rb (a), Sr (b), K_2O (c), Na_2O (d), La (e), Ce (f), Th (g), Nb (h) and Yb (i).

Symbols: rhyolite: black filled triangle; amphibole gabbros 17LT09-1, 17LT09-2, 17LT09-3: green filled square; amphibole gabbros 17LT09-5 and 17LT09-6: blue filled circle.

relatively positive correlation with SiO_2.

Rhyolites have high REE contents with total of REE (TREE) abundance of 170–200 ppm. On the chondrite normalized REE diagram (Fig. 7a), they display distinctly enriched LREE and depleted HREE patterns, with high $(La/Yb)_N$ of 5.40–6.71, $(La/Sm)_N$ of 2.23–2.75 and obvious negative Eu anomalies (Eu_N/Eu_N*= Eu_N/SQRT $(Sm_N \times Gd_N)$=1.03–1.25). On the primitive mantle-normalized trace element spider diagram (Fig. 7b), rhyolites yield negative Nb, Ta, Ti, Sr and P anomalies and positive Zr and Th anomalies.

4.3.3 Whole-rock geochemical compositions for amphibole gabbros

Amphibole gabbros give low SiO_2 (44.1–49.0 wt%) and alkaline compositions (Na_2O+K_2O=1.16–1.98 wt%), high Fe_2O_{3T} (9.16–13.2 wt%), TiO_2 (0.75–1.74 wt%) and MgO (8.16–9.91 wt%) and $Mg^{\#}$ (60–72), and variable Al_2O_3 compositions (11.9–19 wt%). On the Zr/TiO_2 versus Nb/Yb and SiO_2 versus Zr/TiO_2 classification diagrams (Fig. 6a–b), amphibole gabbros fall into sub-alkaline basalt field. On the FeO_T-Na_2O+K_2O-MgO triangular diagram (Fig. 6c), amphibole gabbros distribute along Fe-rich trend that are comparable to tholeiites, which is confirmed by their plots within tholeiitic areas on the FeO_T/MgO versus SiO_2 diagram (Fig. 6d). On the SiO_2 versus major element compositions (Fig. 6e–f, not all shown), Al_2O_3, Fe_2O_{3T}, Na_2O and TiO_2 all display negative correlations with SiO_2.

On the chondrite normalized REE diagram (Fig. 7c), amphibole gabbros are slightly depleted in La and Ce and yield relatively flat MREE and HREE patterns, with $(Gd/Yb)_N$ of 1.39–2.02, among which samples 17LT09-1, 17LT09-2 and 17LT09-3 yield relatively high REE contents with TREE of 61–107 ppm, $(La/Sm)_N$ of 0.79–1.07, $(La/Yb)_N$ of 1.89–2.86 and obviously negative Eu anomalies (Eu_N/Eu_N*=0.70–0.86). The remained samples 17LT09-5 and 17LT09-6 give broadly lower REE compositions (TREE=40–56 ppm) and lower $(La/Sm)_N$ of 0.45–0.51 and $(La/Yb)_N$ of 0.70–1.02, accompanied with mild to no Eu anomalies (Eu_N/Eu_N*=0.90–1.14). On the primitive mantle normalized trace element diagram (Fig. 7d), all amphibole gabbros exhibit negative Nb, Ta, Zr and Hf anomalies. However, compared to amphibole gabbros with high REEs, samples 17LT09-5 and 17LT09-6 yield obviously lower Nb and Ta contents.

5 Discussion

5.1 Petrogenesis and tectonic implications for the Zhalantun Paleozoic rocks

5.1.1 Petrogenesis and tectonic implication of rhyolite

Rhyolites in the study area exhibit high siliceous and

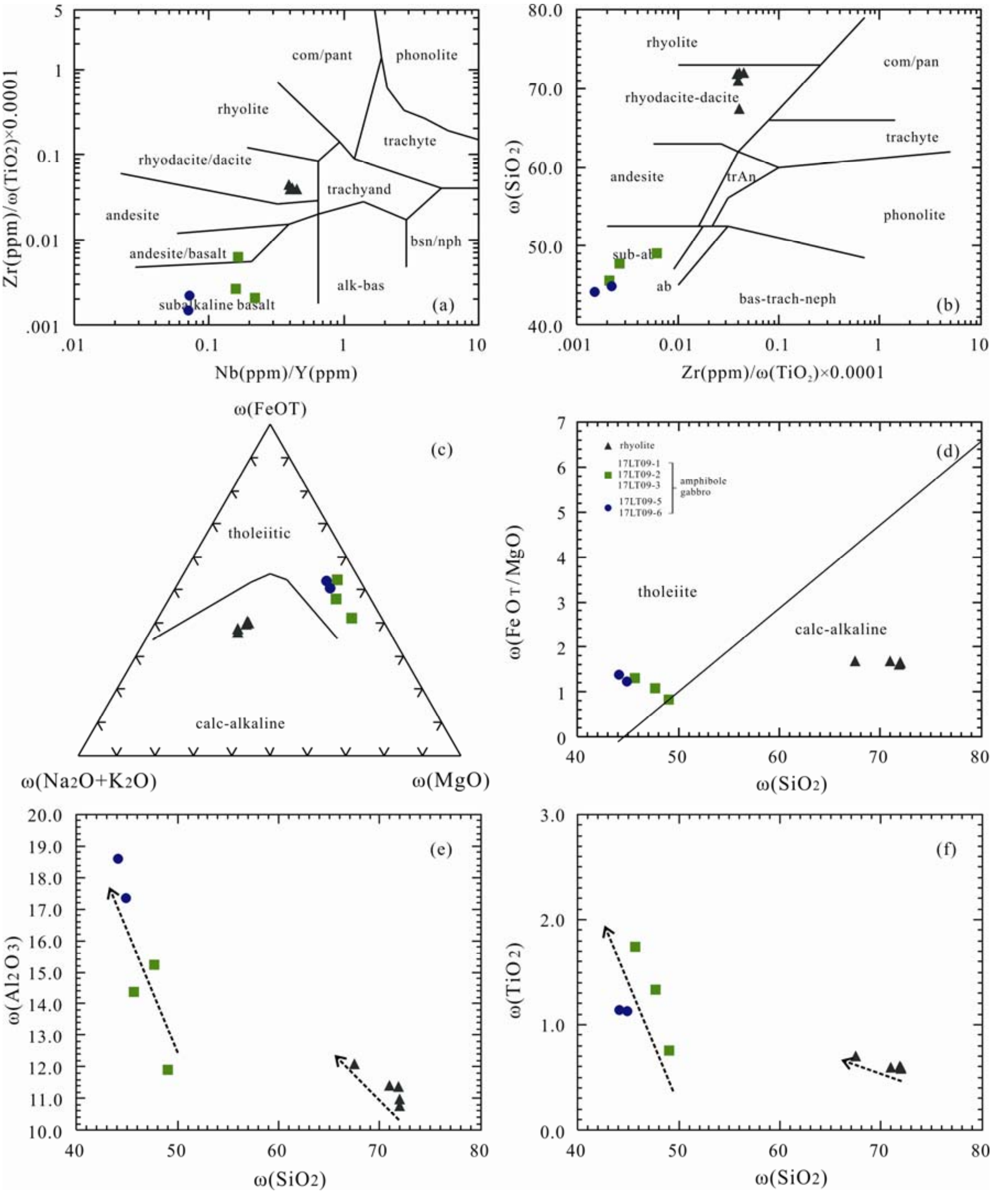

Fig. 6. (a) Zr/TiO_2 versus Nb/Y classification diagram (after Winchester and Floyd, 1977). (b) SiO_2 versus Zr/Ti diagram (after Winchester and Floyd, 1977). (c) FeO_T- Na_2O+K_2O-MgO triangular diagram. (d) FeO_T/MgO versus SiO_2 diagram (after Myashiro, 1974). (e) Al_2O_3 versus SiO_2 diagram; (F) TiO_2 versus SiO_2 diagram. Symbols are the same as in Fig. 5.

alkaline contents but lower TiO_2 contents, indicative of crustal affinities. Most Lu-Hf analyses plot below the CHUR line, further proving that crustal melts were mainly dominated their magma source. The AMF vs. CMF diagram and $CaO/(FeO_T+MgO+TiO_2)$ vs. $FeO_T+CaO+MgO+TiO_2$ diagram (Fig. 8a–b), all rhyolites plot within melts of meta-basalt/amphibolites, implying that they are derived from the partial melting of ancient basalts. Experimental petrology reveals that melts from the lower continental crust (LCC) yield $Mg^{\#}$ generally less than 45. The $Mg^{\#}$ versus SiO_2 diagram (Fig. 8c) further limits the scope for melts of meta-basalt and eclogite (representative LCC compositions). Rhyolites from the Zhalantun basements yield relatively high MgO (2.53–3.03 wt.%) and $Mg^{\#}$ (55–56), and therefore plot above the LCC scope on the Fig. 8c. Furthermore, several zircon Lu-

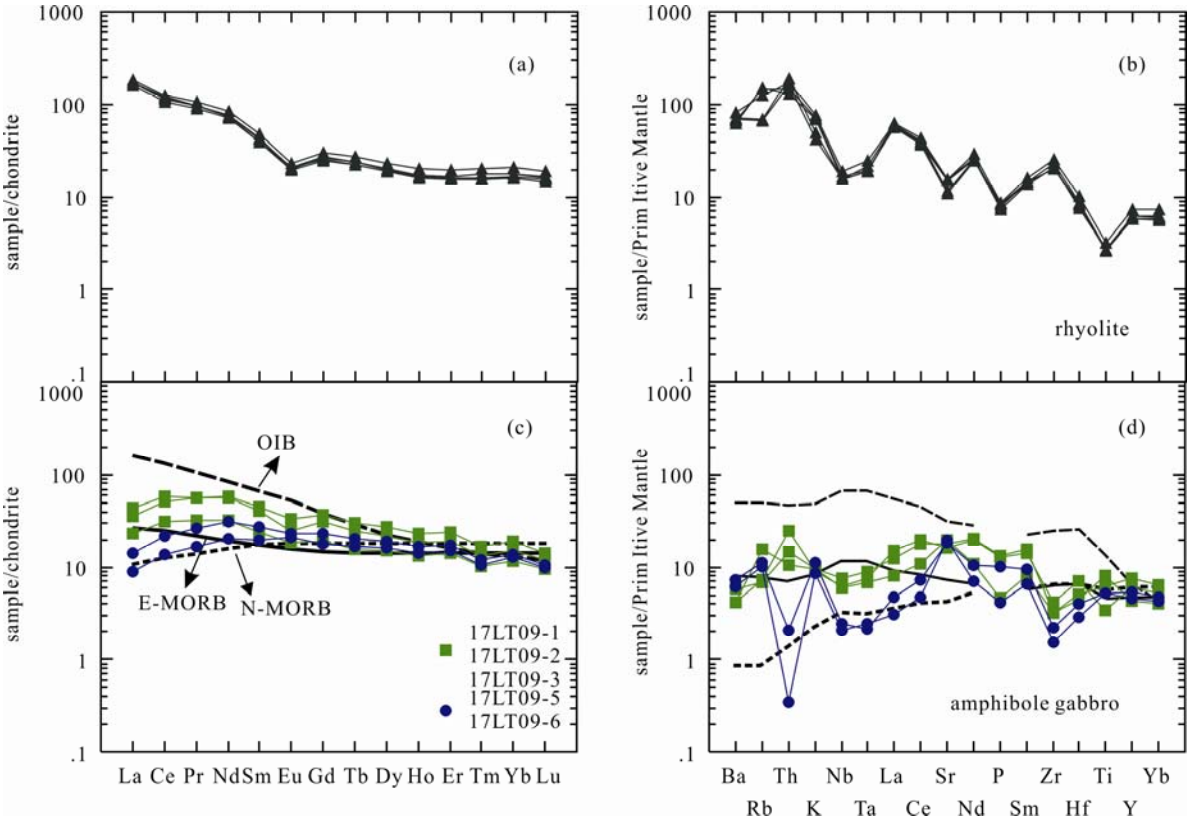

Fig. 7. Chondrite-normalized REE patterns and primitive mantle-normalized multi-element spider diagrams.
The symbols are the same as in Fig. 5. The normalization values and the data for N-MORB, E-MORB and OIB are after Sun and McDonough (1989). Abbreviations: N-MORB: Normal-type Mid-Ocean Ridge Basalt; E-MORB: Enriched-type Mid-Ocean Ridge Basalt; OIB: Ocean Island Basalt.

Hf analyses from rhyolites plot between CHUR and DM lines. Thus, mantle compositions attributed to parental magmas of rhyolites as well. Taken together, rhyolites in this study were derived from partial melting of crustal basalts contaminated by depleted mantle compositions. The negative Eu and Sr anomalies (Fig. 7a) suggest that plagioclase was one of the main fractional crystallization phases. The horizontal line constructed by rhyolites on the Dy/Yb versus SiO_2 diagram (Fig. 8e) imply that amphibole was not the major phase involving the fractional crystallization, which is consistent with the paucity of MREE depletion for rhyolites. Besides, the positive correlation between La and $(La/Yb)_N$ suggest that REE compositions of rhyolites were effected by fractional crystallization of monazite.

The Zhalantun rhyolites are characterized by highly enrichments of LILEs and LREEs, and depletions of HFSEs (Fig. 7a), comparable to typical Phanerozoic island arc magmas (e.g. Wang et al., 2017, 2016, 2015b). On the Nb–Y tectonic classification diagram (Fig. 9a), all rhyolites fall into volcanic arc granite/syn-collisional granite field. Furthermore, all rhyolites plot into continental margin arc setting on the Th_N–Nb_N (Fig. 9b), further proving their continental arc affinity. Considering certain xenocryst zircons captured by rhyolites, we prefer to interpret rhyolites as products of continental arc, instead of oceanic arc.

Taken together, rhyolites in the Zhalantun were derived from partial melting of crustal basalts induced by upwelling of sub-arc depleted mantle materials, and subsequently underwent fractional crystallization of plagioclase.

5.1.2 Petrogenesis and tectonic implication of amphibole gabbros

Amphibole gabbros in the Zhalantun yield high MgO of 8.16–9.91 wt% and $Mg^{\#}$ of 60–72, but low Zr (17–47 ppm) contents, indicative of a dominant mantle source, which is consistent with plots within and around mantle-melt field on the $Mg^{\#}$ - SiO_2 diagram (Fig. 8c). On the εHf (t) versus Age diagram (Fig. 4f), amphibole gabbro 17LT09-3 mainly fall between Depleted mantle and CHUR lines while some plot below the CHUR line, implying a dominant mantle source and later contaminations by continental crust. However, element Zr of amphibole gabbros does not inversely correlated to Nb and MgO (Fig. 5h), suggesting that the degree of assimilations by continental crust was limited.

Amphibole gabbros 17LT09-5 and 17LT09-6 are distinguished from the remained gabbros 17LT09-1, 17LT09-2, and 17LT09-3 by slightly lower LREE abundances and markedly lower Nb and Ta contents. However, on the SiO_2 versus major oxides diagrams and Zr versus trace element diagrams (Fig. 5), regarding to Al_2O_3, Fe_2O_{3T}, Na_2O, $Mg^{\#}$, Sr, La, Ce, Yb and Nb, these low-HFSE samples (17LT09-5 and 17LT09-6) define good

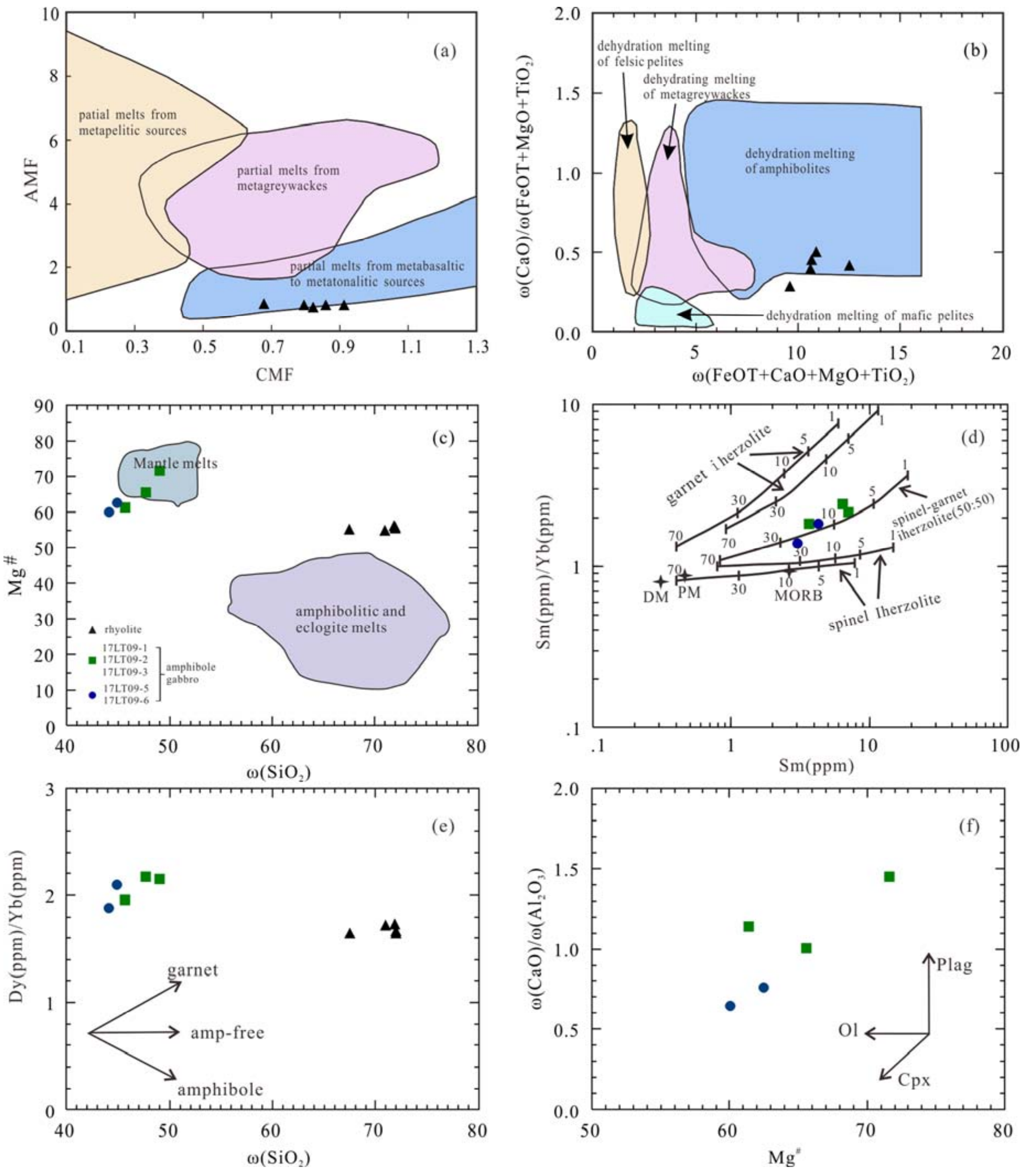

Fig. 8. (a) Molar $Al_2O_3/(MgO+FeO_T)$ (AFM) versus $CaO/(MgO+FeO_T)$ (CFM) diagram (modified after Altherr et al., 2000); (b) $CaO/(FeO_T+MgO+TiO_2)$ versus $CaO+FeO_T+MgO+TiO_2$ diagram (after Patiño Douce, 1999); (c) $Mg^{\#}$ versus SiO_2 diagram (after Stern and Killian, 1996). The fields of experimental pure crustal partial melts by dehydration melting of amphibolitic and eclogite melts are modified by Rapp et al. (1999) and Smithies (2000); (d) Sm/Yb versus Sm diagram (after Aldanmaz et al., 2000); (e) Dy/Yb versus SiO_2 diagram (after Davidson et al., 2007); (f) CaO/Al_2O_3 versus $Mg^{\#}$ diagram.

Abbreviations: DM: depleted mantle; OIB: oceanic island basalt; N-MORB: Normal-type mid-ocean ridge basalt; E-MORB: Enriched-type mid-ocean ridge basalt; Amp: amphibole; Ol: olivine; Plag: plagioclase; Cpx: clinopyroxene.

linear correlations with remained high-HFSE amphibole gabbros (17LT09-1, 17LT09-2 and 17LT09-3). Rb, K_2O and Th display dispersive plots due to element mobility as mentioned in section 4.3.1. The scattered TiO_2 (Fig. 6e) might be caused by titanite exposed in high-HFSE amphibole gabbros which result in slightly elevated Nb and Ta contents in high-HFSE samples. Therefore, all amphibole gabbros follow typical igneous evolutionary trends for most major and trace element compositions. On the other hand, though low-HFSE samples (17LT09-5 and 17LT09-6) exhibit lower LREE and HFSE compositions, all amphibole gabbros yield coherent and similar REE and trace element patterns on the chondrite-normalized REE and primitive mantle-normalized trace element diagrams (Fig. 7c–d). Besides, all amphibole gabbros were collected from the same one pluton. Taken together, the Zhalantun amphibole gabbros in this study were derived from a same original mantle source. The diverse LREE and HFSE abundances are likely related to different degrees of partial melting and various minerals involved in fractional crystallization and/or accumulation.

The depleted LREE and distinct Nb-Ta negative anomalies of amphibole gabbros exclude OIB and E-MORB affinities which are characterized by enrichments in LREE and no or insignificant Nb negative anomalies. The left-declined REE patterns and low $(La/Sm)_N$ ratios of 0.45–1.07 are akin to N-MORB (Fig. 7c). On the other hand, the enriched LILEs and depleted Nb, Ta, Zr compositions of these mafic rocks are different from N-MORB but consistent with Phanerozoic arc magmatism. It is worth noting that Nb and Ta negative anomalies can be caused by assimilations from continental crust as well. However, markedly negative Zr anomalies, high MgO and $Mg^{\#}$ and low SiO_2 contents suggest that contaminations by continental crust was limited. Therefore, the depleted HFSEs of the Zhalantun amphibole gabbros reflect their primary compositions. Furthermore, arc gabbros generally yield Nb/Th ratios < 7.5 while non-arc gabbros give Nb/Th >8.5 (Jenner et al., 1991). These gabbros in the Zhalantun have Nb/Th values of 2.13–4.83 except samples 17LT09-5 and 17LT09-6 with abnormal Th abundances, implying these amphibole gabbros are closely related to arc magmatism. Therefore, the negative Nb, Ta anomalies and enrichments of LILEs of amphibole gabbros were probably originated from partial melting of sub-arc mantle previously metasomatized by down-going slab-derived fluids/melts. Their slightly depleted LREE and unfractionated HREE patterns further suggest a shallow mantle source with the involvement of a deep MORB-like compositions. All amphibole gabbros plot on the spinel-garnet lherzolite (50:50) curve on the Sm/Yb versus Sm diagram (Fig. 8d), indicative of spinel and garnet minerals coexisting in a relatively shallow mantle source. Samples 17LT09-5 and 17LT09-6 yield mildly lower Sm/Yb and Sm values on Fig. 8c and underwent higher degrees of partial melting than the remained three mafic rocks, which is in accordance with their lower LREE and $(La/Sm)_N$ contents. The high-HFSE samples yield evident negative Eu anomalies with Eu_N/Eu_N* values of 0.70–0.86, indicative of fractional crystallization of plagioclase, while low-HFSE amphibole gabbros give negligible to positive Eu anomalies and obviously positive Sr anomalies, pointing to accumulations of plagioclase. Additionally, minor accumulations of plagioclase are in conformity with mildly higher Al_2O_3 abundances for samples 17LT09-5 and 17LT09-6. High-HFSE mafic rocks consist of accessory minerals of titanite which therefore result in their relatively higher Nb, Ta and TiO_2 contents (Figs. 6f and 7d, Table 4). All amphibole gabbros define positive correlations between Dy/Yb and SiO_2 and between CaO/Al_2O_3 and $Mg^{\#}$ (Fig. 8e–f), indicative of fractional crystallization of garnet and clinopyroxene.

The subduction-related magmatisms recorded by these mafic rocks exclude the possibility of an intra-continent environment and imply that they formed under an active continental margin. This can be further examined through plots within continental arc field, though samples 17LT09-5 and 17LT09-6 display considerable scatter due to their Th mobility (Fig. 9b). Additionally, both N-MORB-like and arc-like characteristics are generally limited to back arc regime. Back arc basin basalt (BABB) yield either MORB-like signatures with slight LREE depletion, negligible LILE enrichment and HFSE depletion, or transitional geochemical compositions between MORB and arc magmas with distinct enriched LILE and depleted HFSE. The geochemical characteristics of BABB are generally controlled by spatial relation between arc and back-arc systems (Manikyamba et al., 2015, 2009; Gribble et al., 1996). On Ti/V–Zr and Y–La–Nb tectonic classification diagrams (Fig. 9c–d), the spots of the Zhalantun amphibole gabbros plot through arc and BABB fields while mostly fall within/close to BABB scope, probably ascribed to different degrees of mixture between arc-like and N-MORB-like components. Moreover, ~430 Ma gabbros in the Yalu area and ~469 Ma meta-basalts of the Aershan area were both interpreted as back-arc products as well (Feng et al., 2018; Wang, 2015).

Taken together, the Zhalantun amphibole gabbros were formed within a back-arc basin tectonic setting. Both sub-arc mantle and N-MORB-like mantle contributed to their parental magmas. Subsequently, these mafic magmas underwent fractional crystallization of clinopyroxene, garnet and plagioclase, or minor accumulation of plagioclase and titanite.

5.2 Geochronology and tectonic implications of the supposed Zhalantun Precambrian basement

In the last century, geologists interpreted the Zhalantun basements as Proterozoic products according to regional stratum comparison and whole-rock Rb-Sr and Sm-Nd isotopic dating (IMBGRM, 1991). At the beginning of the 21st century, gabbros and quartz monzonites from the Zhalantun were reported to be Proterozoic intrusions by single zircon evaporation method (He et al., 2006). However, Rb and Sr are alteration sensitive elements, resulting in relatively poor accuracy. Besides, less than ten zircon grains were dated for each sample by He et al. (2006), lacking statistical significance. Therefore, whether the Precambrian basements outcrop in the Zhalantun or not has been questionable.

In this study, we collected supposed Proterozoic supracrustal rocks including rhyolites, muscovite schist and siltstone, and plutons, like amphibole gabbros and diorite, for zircon in-situ dating. The geochronological results reveal that rhyolite formed at 505±5 Ma, muscovite schist (meta-sedimentary rock) and siltstone generated after 499±4 Ma and 489±4 Ma, respectively, and amphibole gabbros and diorite crystallized at 447±6 Ma and 125±1 Ma, respectively. Therefore, the previously believed Proterozoic supracrustal rocks and plutons are proved to be Paleozoic and Mesozoic products.

Coincidentally, other researchers also reported several Paleozoic to Mesozoic ages from the supposed Zhalantun Precambrian basements, which are summarized in Table 5.

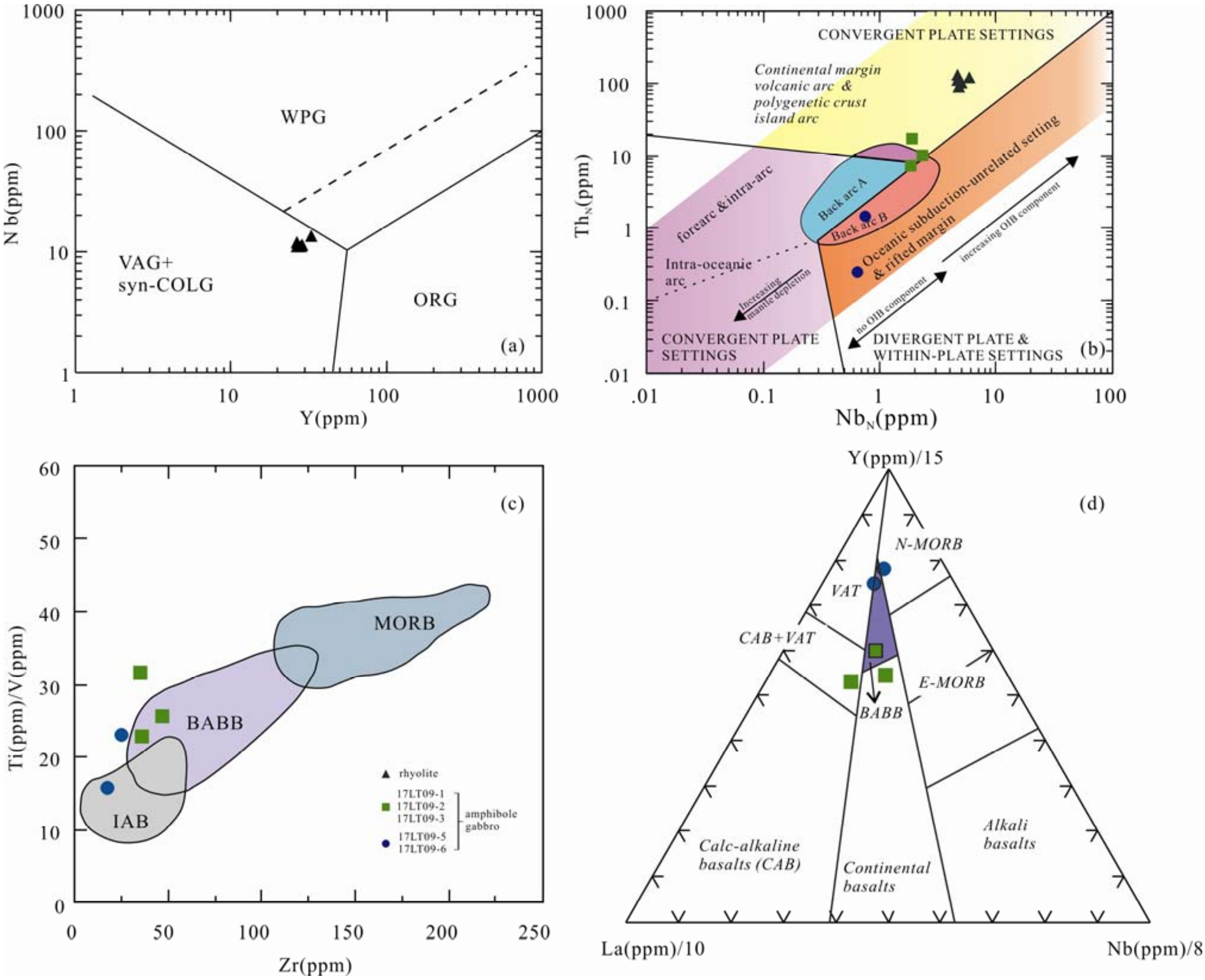

Fig. 9. (a) Nb versus Y diagram (after Pearce, 1996). (b) Th_N versus Nb_N (after Saccani, 2015). The Th and Nb are normalized to the N-MORB composition (Sun and McDonough, 1989). Back-arc A indicates that the BABBs are characterized by the input of subduction or crustal components, whereas Back-arc B indicates that the BABBs show no additions of subduction or crustal components. (c) Ti/V versus Zr diagram (after Gribble et al., 1996). (d) Y-La-Nb triangular diagram (after Cabanis and Lecolle, 1989).
Abbreviations: WPG: within-plate granite; ORG: ocean range granite; VAG: volcanic arc granite; COLG: collisional granite; BABB: back-arc basin basalt; IAB: island arc basalt; CAB: calc-alkaline basalt.

For example, chlorite schists, muscovite schist and quartz sandstones from the Zhalantun and Arongqi areas recorded the youngest age peaks of ~513 Ma, ~497 Ma, ~519 Ma and ~477 Ma (Yang, 2007). A meta-basalt was considered to erupt at ~506 Ma (Miao et al., 2007). Zhou et al. (2014) reported that the maximum depositional age of a chlorite schist from the Zhalantun area was around ~481 Ma. Dacite, meta-basalt and chlorite actinolite schist from the Aershan generated at ~475 Ma, ~469 Ma and ~464 Ma, respectively, among which meta-basalts recorded back-arc magmatism (Wang, 2015). Phyllite and mica schists from the Chaihe town of the Zhalantun area deposited after ~429–412 Ma and were related to active continental margin (Cui et al., 2015). Guo et al. (2009) reported that Dashizhai basalts formed at ~439 Ma and generated under fore arc-arc environment. Therefore, the alleged Proterozoic Zhalantun basements were proved to be Phanerozoic products, instead of Proterozoic.

Taken together, none Precambrian lithological records have been reported in the Zhalantun so far. The previously believed Proterozoic basements are conversely proved to be Paleozoic and Mesozoic rocks. The Paleozoic rocks in the Zhalantun mainly consists of meta-basalts, meta-andesites, rhyolites, gabbros, and (meta-) sedimentary rocks, like chlorite schist, quartz sandstone, siltstone, actinolite schist and biotite schist, with formation ages focus at ~510 Ma, ~440–460 Ma and ~410 Ma. These Paleozoic rocks were believed to be formed under subduction-related regime (Cui et al., 2015; Yang et al., 2007), though the subduction polarity, numbers and locations of arc activities remain unknown. The Mesozoic rocks recognized from the Zhalantun Precambrian basements are mainly quartz diorites with an age of ~125 Ma.

On the other hand, though none Precambrian rocks have been recognized, a number of Proterozoic to Archean

Table 5 Summarized Phanerozoic ages reported from the alleged Proterozoic ZLT basements

Lithology	Location	Latitude	Longitude	Age	Ancient xenocryst/detrial zircon ages	References
Rhyolite	Zhalantun-Woniuhe	47°55'30"N	122°25'39"E	CA: 505±5 Ma	~600-700 Ma, ~800-970 Ma, ~1600-2220 Ma, ~2400 Ma ~2600 Ma, ~2700 Ma, ~2860 Ma	This paper
chloritization muscovite schist		48°04'25"N	122°30'50"E	MDA: 499±4 Ma		
Siltstone		47°58'34"N	122°31'45"E	MDA: 489±4 Ma		
Amphibole gabbro	Northeastern Dabeigou	48°36'32"N	122°03'46"E	CA: 447±6 Ma		
Quartz diorite	Zhalantun-Woniuhe	48°04'26"N	122°31'00"E	CA: 125±1 Ma		
chlorite muscovite schist	Zhalantun-Woniuhe	48°06'31″N	122°37'22″E	MDA: ~519 Ma	~700-900 Ma, ~1600-1900 Ma, ~2200-2440 Ma, ~2800 Ma, ~3100 Ma, ~3210 Ma	Yang, 2007
calcite chlorite schist		48°04'56″N	122°40'39″E	MDA: ~497 Ma		
Muscovite chlorite schist		48°06'12″N	122°46'00″E	MDA: ~513 Ma		
Meta-feldspar quartz sandstone	Molidawa	48°33'59″N	124°15'31″E	MDA: ~477 Ma		
Chlorite schist	Xiangyangyu	48°01'43″N	123°17'35″E	MDA: ~481 Ma	~820 Ma, ~1400 Ma, ~2000 Ma, ~2300 Ma, ~2660 Ma, ~2930 Ma	Zhou et al., 2014
Meta-basalt	Yimin River	47°20'47″N	120°58'53″E	CA: ~469 Ma	~730 Ma, ~900-1000 Ma, ~2200 Ma, ~2500 Ma	Wang, 2017
Meta-dacite		47°44'13″N	120°51'40″E	CA: ~475 Ma		
Meta-basalt		47°56'14″N	120°26'14″E	CA: ~464 Ma		
chlorite schist (meta-basalt)	Northeastern Zhalantun	48°03'51″N	123°07'16″E	CA: ~506 Ma		Miao et al., 2007
Mica schist	Chaihe-Taerqi	47°33'45″N	120°15'38″E	MDA: 416±1 Ma	~680 Ma, ~760 Ma, ~800-960 Ma	Cui et al., 2015
Meta-sandstone		47°33'13″N	120°17'03″E	MDA: 414±9 Ma		
Mica schist		47°33'45″N	120°15'37″E	MDA: 412±3 Ma		
Phyllite		47°24'12″N	120°12'18″E	MDA: 429±4 Ma		
Basalt	Dashizhai			CA: ~439 Ma		Guo et al., 2009

Abbreviations: CA: crystallization age; MDA: maxium depositional age

detrital/xenocryst zircons have been reported. For example, detrital zircons with ages of ~700 – 1000 Ma, ~1400–1900 Ma, ~2200–2400 Ma, ~2600 Ma, ~2700 Ma, ~2800 Ma and ~3200 Ma have been recognized in rhyolites, amphibole gabbros, chlorite schist, siltstone and muscovite schist, feldspar quartz sandstone and lithic arkose (Yang, 2007; Zhou et al., 2014; Wang, 2017; Cui et al., 2015). Some researchers purposed that these ancient detrital zircons might migrate from neighboring Erguna Massif to the west and the Songnen-Zhangguangcai Rang Massif to the east, instead of local Zhalantun (Li et al., 2017). However, such ancient zircon ages were also recognized from igneous rocks, like rhyolites and meta-mafic rocks (amphibole gabbro) in this study, indicative of local ancient zircons. Furthermore, Zhang et al. (2017) and Qian et al. (2018) reported ~2.5 Ga and 1.8 Ga granites in the Longjiang area, south of Zhalantun. Therefore, Precambrian rocks once outcropped in the Zhalantun while they were probably re-worked and were consumed during later long evolutionary history, giving rise to widely absence of Precambrian rock records.

6 Conclusions

(1) Rhyolite, amphibole gabbro and quartz diorite from the supposed Proterozoic Zhalantun basements formed at 505±5 Ma, 447±6 Ma and 125±1 Ma, respectively. The supposed Proterozoic muscovite schist and siltstone yield maximum depositional ages of 499±4 Ma and 489±4 Ma, respectively. Several ancient detrital/xenocryst zircons were still recorded with ages of ~530–660 Ma, ~750–1000 Ma, ~2400 Ma and ~2600–2860 Ma.

(2) The ~505 Ma rhyolites were derived from partial melting of continental basalts induced by upwelling of sub-arc mantle magmas, and subsequently underwent fractional crystallization of plagioclase, which were probably related to continental arc regime.

(3) The ~447 Ma amphibole gabbros were generated within a back-arc basin tectonic setting. Their parental magmas were contributed by both sub-arc mantle and N-MORB-like mantle. During magma ascent, they experienced fractional crystallization of clinopyroxene, garnet and plagioclase, or minor accumulation of plagioclase and titanite, accompanied with limited assimilations by continental crust.

(4) The supposed Proterozoic Zhalantun supracrustal rocks and plutons which have been proven to be Paleozoic and Mesozoic rocks. These Paleozoic rocks were generally formed in subduction-related regime with three pulses of magmatism at ~510 Ma, ~440 – 460 Ma and ~410 Ma. The Mesozoic rocks are mainly focused on ~125 Ma. Taken together, none Proterozoic rocks have been identified from the Zhalantun Precambrian basements, though several ~500 – 2800 Ma detrital and xenocryst zircons were captured. Combined with reported ancient zircon ages and newly discovered ~2.5 Ga and ~1.8 Ga granites from the south of the Zhalantun, the Precambrian rocks probably once exposed in the Zhalantun which were re-worked and consumed during later long tectonic evolutionary history, resulting in absence of Precambrian rocks in the Zhalantun.

Acknowledgements

We would like to thank Dr. Shan Li and three anonymous reviewers for their helpful comments, which highly improved this manuscript. We also appreciate Dr. Lishuang Guo for whole-rock geochemical analyses at the

Institute of Crustal Dynamics, China Earthquake Administration, Dr. Pengyuan Guo for zircon U-Pb dating at the Institute of Oceanology, Chinese Academy of Sciences, and Dr. Guibin Zhang for zircon Lu-Hf isotopic analyses at the Peking University. This study is financially supported by China Geological Survey Project (Grant Number: DD20190039-01, DD20160048-01) and the Fundamental Research Funds for the Central Universities (Grant Number: N160104003).

Manuscript received May 15, 2019
accepted Aug. 14, 2019
associate EIC XIAO Wenjiao
edited by FEI Hongcai

References

Altherr, R., Holl, A., Hegner, E., 2000. High-potassium, calc-alkaline I-type plutonism in the European Variscides: Northern Vosges (France) and northern Schwarzwald (Germany). Lithos, 50: 51–73.

Aldanmaz, E., Pearce, J.A., Thirlwall, M.F., and Mitchell, J.G., 2000. Petrogenetic evolution of late Cenozoic post-collision volcanism in western Anatolia, Turkey. Journal of Volcanology and Geothermal Research, 102: 67–95.

Cabanis, B., and Lecolle, M., 1989. Le diagramme La/10-Y/15-Nb/8: un outil pour la discrimination des series volcanique et la mise en evidence des processus de melange et/ou de contamination crustale. C.R. Acad. Sci. Ser, II, 309: 2023–2029.

Cui, F., Zheng, C., Xu, X., Yao, W., Ding, X., Shi, L., and Li, J., 2015. Detrital zircon ages of the Jiageda and Woduhe formations: constrains on the tectonic attribute of the Xing'an terrane in the central Great Xing'an Range, NE China. Journal of Asian Earth Sciences, 113: 427–442.

Dai, J., Wang, C., Hébert, R., Li, Y., Zhong, H., Guillaume, R., Bezard, R., and Wei, Y., 2011. Late Devonian OIB alkaline gabbro in the Yarlung Zangbo suture zone: Remnants of the Paleo-Tethys? Gondwana Research, 19: 232–243.

Davidson J, Turner S, Handley H, Macpherson C, and Dosseto A., 2007. Amphibole "sponge" in arc crust? Geology, 35: 787–790.

Defant, M.J., and Drummond, M.S., 1990. Derivation of some modern arc magmas by melting of young subducted lithosphere. Nature, 347: 662–665.

Defant, M.J., Jackson, T.E., Drummond, M.S., De Boer, J.Z., Bellon, H., Feigenson, M.D., Maury, R.C., and Stewart, R.H., 1992. The geochemistry of young volcanism throughout western Panama and southeastern Costa Rica: an overview. Journal of the Geological Society, 149: 569–579.

Dong, Y., Ge, W., Zhao, G., Yang, H., Liu, X., and Zhang, Y., 2016. Petrogenesis and tectonic setting of the Late Paleozoic Xing'an complex in the northern Great Xing'an Range, NE China: Constraints from geochronology, geochemistry and zircon Hf isotopes. Journal of Asian Earth Sciences, 115: 228–246.

Feng, Z.Q., Jia, J., Liu, Y.J., Wen, Q., Li, W.M., Liu, B., Xing, D., and Zhang, L., 2015. Geochronology and geochemistry of the Carboniferous magmatism in the northern Great Xing'an Range, NE China: Constraints on the timing of amalgamation of Xing'an and Songnen blocks. Journal of Asian Earth Sciences, 113: 411–426.

Feng, Z.Q., Liu, Y.J., Wu, P., Jin, W., Li, W.M., Wen, Q.B., Zhao, Y.L., and Zhou, J.B., 2018. Silurian magmatism on the eastern margin of the erguna block, ne china: evolution of the northern great xing'an range. Gondwana Research, 61: 46–62.

Ge, W.C., Sui, Z.M., Wu, F.Y., Zhang, J.H., Xu, X.C., and Cheng, R.Y., 2007. Zircon U–Pb ages, Hf isotopic characteristics and their implications of the Early Paleozoic granites in the northeastern Da Hinggan Mts, northeastern China. Acta Petrologica Sinica, 23: 423–440 (in Chinese with English abstract).

Gribble, R.F., Stern, R.J., Bloomer, S.H., Stüben, D., O'Hearn, T., and Newman, S., 1996. MORB mantle and subduction components interact to generate basalts in the southern Mariana Trough back-arc basin. Geochim. Cosmochim. Acta, 60: 2153–2166.

Guo, F., Fan, W.M., Li, C.W., Miao, L.C., and Zhao, L., 2009. Early Paleozoic subduction of the Paleo-Asian Ocean: Geochronological and geochemical evidence from the Dashizhai basalts, Inner Mongolia. Science China, 39: 569–579 (in Chinese with English abstract).

Guo, P., Niu, Y., Sun, P., Wang, X., Gong, H., Duan, M., Zhang, Y., Kong, J., Tian, L., and Wu, S., 2018. The Early Cretaceous bimodal volcanic suite from the Yinshan Block, western North China Craton: Origin, process and geological significance. Journal of Asian Earth Sciences, 160: 348–364.

Guo, R., Liu, S., Gong, E., Wei, W., Wang, M., Fu, J., and Qin, T., 2017a. Arc-generated metavolcanic rocks in the Anshan–Benxi greenstone belt, north china craton: constraints from geochemistry and zircon u–pb–hf isotopic systematics. Precambrian Research, 303: 228–250.

Guo, R., Liu, S., Xiang, B., and Wei, W., 2017b. A Neoarchean subduction recorded by the eastern Hebei Precambrian basement, north china craton: geochemical fingerprints from metavolcanic rocks of the Saheqiao-Shangying-Qinglong supracrustal belt. Journal of Asian Earth Sciences, 135: 347–369.

Guo, R., Liu, S., Wyman, D., Bai, X., Wang, W., Yan, M., and Li, Q., 2015. Neoarchean subduction: a case study of arc volcanic rocks in Qinglong-Zhuzhangzi area of the Eastern Hebei Province, North China Craton. Precambrian Research, 264: 36–62.

Guo, R., Liu, S., Santosh, M., Li, Q., Bai, X., and Wang, W., 2013. Geochemistry, zircon U–Pb geochronology and Lu–Hf isotopes of metavolcanics from eastern Hebei reveal Neoarchean subduction tectonics in the North China Craton. Gondwana Research, 24: 664–686.

He, H.W., Wu L.W., Zhang, M., Guo, L.J., Gong G.B., Zheng, W.J., Zhang, Z.Z., Guo, W.J., Xu, Z., Xu, and Y.W., 2006. 1:250 000 Zhalantun regional geological survey report. Inner Mongolia Geological Survey Institute, Inner Mongolia, pp:1–293 (in Chinese).

IMBGRM (Inner Mongolian Bureau of Geology Mineral Resources), 1991. Regional Geology of Inner Mongolia. Geological Publishing House, Beijing, pp: 1–725 (in Chinese with English abstract).

Jahn, B. M., 2000. Massive granitoid generation in Central Asia: Nd isotope evidence and implication for continental growth in the Phanerozoic. Episodes, 23: 82–92.

Khanchuk, A.I., Didenko, A.N., Popeko, L.I., Sorokin, A.A., and Scevchenko, B.F., 2015. Structure and evolution of the Mongol–Okhotsk Orogenic Belt. In: Kroner, A. (Ed.), The Central Asian Orogenic BeltContributions to the Regional Geology of the Earth. E. Schweitzerbart Science Publishers, Stuttgart, Germany, pp: 211–234.

Kozakov, I.K., Sal'nikova, E.B., Wang, T., Didenko, A.N., Plotkina, Y.V., and Podkovyrov, V.N., 2007. Early Precambrian crystalline complexes of the Central Asian microcontinent: age, sources, tectonic position. Stratigraphy and Geological Correlation, 15:121–140.

Kröner, A., Demoux, A., Zack, T., Rojas-Agramonte, Y., Jian, P., Tomurhuu, D., and Barth, M., 2011. Zircon ages for a felsic volcanic rock and arc-related early Palaeozoic sediments on the margin of the Baydrag microcontinent, central Asian orogenic belt, Mongolia. Journal of Asian Earth Sciences, 42: 1008–1017.

Li, S., Wilde, S.A., Wang, T., and Xiao W.J., 2016. Latest Early Permian granitic magmatism in southern Inner Mongolia, China: Implications for the tectonic evolution of the southeastern Central Asian Orogenic Belt. Gondwana Research, 29: 168–180.

Li, S., Wang, T., Wilde, S.A., and Tong, Y., 2013. Evolution, source and tectonic significance of early mesozoic granitoid magmatism in the central asian orogenic belt (central segment). Earth-Science Reviews, 126: 206–234.

Li, Y., Xu, W.L., Tang, J., Pei, F.P., Wang, F., and Sun, C.Y., 2018. Geochronology and geochemistry of Mesozoic intrusive rocks in the Xing'an Massif of NE China: Implications for the evolution and spatial extent of the Mongol–Okhotsk tectonic regime. Lithos, 304: 57–73.

Li, Y., Xu, W.L., Wang, F., Pei, F.P., Tang, J., and Zhao, S., 2017. Triassic volcanism along the eastern margin of the Xing'an Massif, NE China: Constraints on the spatial–temporal extent of the Mongol–Okhotsk tectonic regime. Gondwana Research, 48: 205–223.

Liu, H., Li, Y., He, H., Huangfu, P., and Liu, Y., 2018. Two-phase southward subduction of the Mongol-Okhotsk oceanic plate constrained by Permian-Jurassic granitoids in the Erguna and Xing'an massifs (NE China). Lithos, 304: 347–361.

Liu, K., Zhang, J., Wilde, S.A., Zhou, J., Wang, M., Ge, M., Wang, J., and Ling, Y., 2017. Initial subduction of the Paleo-Pacific Oceanic plate in NE China: Constraints from whole-rock geochemistry and zircon U–Pb and Lu–Hf isotopes of the Khanka Lake granitoids. Lithos, 274: 254–270.

Liu, S., Wang, M., Wan, Y., Guo, R., Wang, W., Wang, K., Guo, B., Fu, J., and Hu, F., 2017. A reworked ~ 3.45 Ga continental microblock of the North China Craton: Constraints from zircon U-Pb-Lu-Hf isotopic systematics of the Archean Beitai-Waitoushan migmatite-syenogranite complex. Precambrian Research, 303: 332–354.

Liu, S., Wang, W., Bai, X., Guo, R., Guo, B., Fu, J., and Wang, M., 2015. Precambrian geodynamics (VII): Formation and evolution of early continental crust. Earth Science Frontiers, 22: 97–108 (in Chinese with English abstract).

Liu, S., Zhang, J., Li, Q., Zhang, L., Wang, W., and Yang, P., 2012. Geochemistry and U–Pb zircon ages of metamorphic volcanic rocks of the Paleoproterozoic Lüliang Complex and constraints on the evolution of the Trans-North China Orogen, North China Craton. Precambrian Research, 222: 173–190.

Liu, Y.J., Zhang, X.Z., Jin, W., Chi, X.G., Wang, C.W., Ma, Z.H., and Zhao, X.F., 2010. Late Paleozoic tectonic evolution in Northeast China. Geologyin China, 37: 943–951. (in Chinese with English abstract).

Liu, Y. J., Zhang, X.Z., Chi, X.G., Wen, Q.B., Liang, C.Y., Han, G.Q., and Zhao,Y.L., 2011. Deformation and tectonic layer division of the upper Paleo-zoic in Daxing'anling area. Journal of Jilin University (Earth ScienceEdition), 41: 1304–1310. (in Chinese with English abstract).

Liu, Y.J., Li, W.M., Feng, Z.Q., Wen, Q.B., Neubauer, F., and Liang, C.Y., 2017. A review of the Paleozoic tectonics in the eastern part ofCentral Asian Orogenic Belt. Gondwana Research, 43:123–148.

Ludwig, K.R., 2003. User's manual for Isoplot 3.00: a geochronological toolkit for Microsoft Excel. Berkeley Geochronology Center Special Publication, vol. 4.

Manikyamba, C., Ganguly, S., Santosh, M., Saha, A., Chatterjee, A., and Khelen, A.C., 2015. Neoarchean arc–juvenile back-arc magmatism in eastern Dharwar Craton, India: Geochemical fingerprints from the basalts of Kadiri greenstone belt. Precambrian Research, 258: 1–23.

Manikyamba, C., Kerrich, R., Khanna, T.C., Satyanarayanan, M., and Krishna, A.K., 2009. Enriched and depleted arc basalts, with Mg-andesites and adakites: A potential paired arc–back-arc of the 2.6 Ga Hutti greenstone terrane, India. Geochimica et Cosmochimica Acta, 73: 1711–1736.

Ma, Y.F., Liu, Y.J., Wang, Y., Tang, Z., Qian, C., Qin, T. Feng, Z.Q., Sun, W., and Zang, Y.Q., 2018. Geochronology and geochemistry of the carboniferous felsic rocks in the central great xing"an range, ne china: implications for the amalgamation history of xing\"an and songliao-xilinhot blocks. Geological Journal, 2018:1–32.

Ma, Y.F., Liu，Y.J., Qin, T., Sun, W., and Zang, Y.Q., 2018. Carboniferous granites in the Jalaid Banner area,middle Great Xing'an Range,NE China: Petrogenesis,tectonic background and orogeny accretionary implications. Acta Petrologica Sinica, 034(10): 2931–2955.

Miao, L.C., Liu, D.Y., Zhang, F.Q., Fan, W.M., Shi, Y.R., and Xie, H.Q., 2007. Zircon SHRIMP U-Pb ages of the "Xinghuadukou Group" in Hanjiayuanzi and Xinlin areas and the "Zhalantun group" in Inner Mongolia, Great Xing'an Range. Chinese Science Bulletin, 51: 591 – 601.

Miao, L.C., Fan, W.M., Zhang, F.Q., Liu, D.Y., Jian, P., Shi, G.H., and Shi, Y.R., 2004. Zircon shrimp geochronology of the xinkailing-kele complex in the northwestern lesser xing'an range, and its geological implications. Chinese Science Bulletin, 49:201–209.

Patiño Douce, A.E., 1999. What do experiments tell us about the relative contributions of crust and mantle to the origin of granitic magmas? Geological Society, London, Special Publications, 168: 55–75.

Pearce, J.A., 1996. Sources and settings of granitic rocks. Episodes, 19: 120–125.

Pei, F.P., Zhang, Y., Wang, Z.W., Cao, H.H., Xu, W.L., Wang, Z.J., Wang, F., and Yang, C., 2016. Early-middle Paleozoic subduction-collision history of the south-eastern central Asian Orogenic Belt: evidence from igneous and metasedimentary rocks of central Jilin Province, NE China. Lithos, 261: 164–180.

Polat, A., 2009. The geochemistry of Neoarchean (ca. 2700Ma) tholeiitic basalts, transitional to alkaline basalts, and gabbros, Wawa Subprovince, Canada: implications for petrogenetic and geodynamic processes. Precambrian Research, 168: 83–105.

Polat, A., and Hofmann, A.W., 2003. Alteration and geochemical patterns in the 3.7–3.8 Ga Isua greenstone belt, West Greenland. Precambrian Research, 126: 197–218.

Qian, C., Chen, H.J., Lu, L., Pang, X.J., Qin, T., Wang, Y., 2018. The discovery of Neoarchean granite in Longjiang area, Heilongjiang Province. Acta Geoscientica Sinica, 39: 27–36.

Rapp, R.P., Shimizu, N., Norman, M.D., and Applegate, G.S., 1999. Reaction between slab-derived melts and peridotite in the mantle wedge: experimental constraints at 3.8 GPa. Chemical Geology, 160: 335–356.

Ren, J.S., Wang, Z.X., and Chen, B.W., 1999. The Tectonics of China from a Global View: A Guide to the Tectonic Map of China and Adjacent Region. Geological Publishing House, Beijing, pp: 1–32.

Rudnick, R., and Gao, S., 2003. Composition of the continental crust. In: Rudnick, R.L. (Ed.), Treatise on Geochemistry, vol. 3. Elsevier-Pergamon Oxford, pp. 1–64.

Saccani, E., 2015. A new method of discriminating different types of post-Archean ophiolitic basalts and their tectonic significance using Th-Nb and Ce-Dy-Yb systematics. Geosci. Front, 6:481–501.

Schiano, P., Monzier, M., Eissen, J.-P., Martin, H., and Koga, K.T., 2010. Simple mixing as the major control of the evolution of volcanic suites in the Ecuadorian Andes. Contributions to Mineralogy and Petrology, 160: 297–312.

Şengör, A. M. C., Natal'In, B. A., and Burtman, V. S., 1993. Evolution of the Altaid tectonic collage and Palaeozoic crustal growth in Eurasia. Nature, 364: 299.

Smithies, R.H., 2000. The Archaean tonalite–trondhjemite–granodiorite (TTG) series is not an analogue of Cenozoic adakite. Earth and Planetary Science Letters, 182: 115–125.

Stern, C.R., and Killian, R., 1996. Role of the subducted slab, mantle wedge and continental crust in the generation of adakites from the Andean Austral Volcanic Zone. Contributions to Mineralogy and Petrology, 123: 263–281.

Sun, G. R., Zhao, H.L., Liu, X.G., Ma, J.S., Han, Y.D., Sha, H.Y., Zhou, S.Q., and Kuang, Y.S., 2005. 1:250 000 Arongqi regional geological survey report. Heilongjiang Geological Survey Institute, Heilongjiang, pp: 1–378 (in Chinese).

Sun, S.s., and McDonough, W.F., 1989. Chemical and isotopic systematics of oceanic basalts: implications for mantle composition and processes. Geological Society, London, Special Publications, 42: 313–345.

Van Achterbergh, E., Ryan, C.G., Jackson, S.E., and Griffin, W.L., 2001. Data reduction software for LA-ICP-MS. Laser-Ablation-ICPMS in the earth sciences—principles and applications. Miner Assoc Can (short course series), 29: 239–243.

Wang, L.M., 2015. Geochemistry of the Ordovician volcanic rocks in Aershan, Inner Mongolia and its tectonic significance. Master Degree Thesis. Changchun: Jilin University (in Chinese with English abstract).

Wang, W., Liu, S., Cawood, P. A., Guo, R., Bai, X., and Guo, B., 2017. Late Neoarchean crust-mantle geodynamics: Evidence from Pingquan complex of the northern Hebei Province,

North China Craton. Precambrian Research, 303: 470–493.
Wang, W., Liu, S., Cawood, P.A., Bai, X., Guo, R., Guo, B., and Wang, K., 2016. Late Neoarchean subduction-related crustal growth in the Northern Liaoning region of the North China Craton: Evidence from ~2.55 to 2.50 Ga granitoid gneisses. Precambrian Research, 281: 200–223.
Wang, W., Tang, J., Xu, W.L., and Wang, F., 2015a. Geochronology and geochemistry of Early Jurassic volcanic rocks in the Erguna Massif, northeast China: Petrogenesis and implications for the tectonic evolution of the Mongol-Okhotsk suture belt. Lithos, 218: 73–86.
Wang, W., Liu, S., Santosh, M., Wang, G., Bai, X., and Guo, R., 2015b. Neoarchean intra-oceanic arc system in the Western Liaoning Province: Implications for Early Precambrian crustal evolution in the Eastern Block of the North China Craton. Earth-Science Reviews, 150: 329–364.
Wilde, S.A., and Zhou, J.B., 2015. The late Paleozoic to Mesozoic evolution of the eastern margin of the Central Asian Orogenic Belt in China. Journal of Asian Earth Sciences, 113: 909–921.
Winchester, J.A., and Floyd, P.A., 1977. Geochemical discrimination of different magma series and their differentiation products using immobile elements. Chemical Geology, 20: 325–343.
Wu, F., Sun, D., Ge, W., Zhang, Y., Grant, M.L., Wilde, S.A., and Jahn, B., 2011. Geochronology of the Phanerozoic granitoids in northeastern China. Journal of Asian Earth Sciences, 41: 1–30.
Wu, F.Y., Li, X.H.,Zheng, Y.F., and Gao, S., 2007. Lu-Hf isotopic systematics and their applications in petrology. Acta Petrologica Sinica, 23: 185-220 (in Chinese with English abstract).
Wu, F., Jahn, B., Wilde, S.A., Lo, C., Yu, T., Lin, Q., Ge, W., and Sun, D., 2003a. Highly fractionated I-type granites in NE China I: geochronology and petrogenesis. Lithos, 66: 241–273.
Wu, F., Jahn, B., Wilde, S.A., Lo, C., Yu, T., Lin, Q., Ge, W., and Sun, D., 2003b. Highly fractionated I-type granites in NE China II: isotopic geochemistry and implications for crustal growth in the Phanerozoic. Lithos, 67: 191–204.
Xiao, W.J., and Santosh, M., 2014. The western Central Asian Orogenic Belt: a window to accretionary orogenesis and continental growth. Gondwana Research, 25: 1429–1444.
Xu, M.J., Xu, W.L., Wang, F., Gao, F.H., and Yu, J.J., 2013a. Geochronology and geochemistry of the Early Jurassic granitoids in the central Lesser Xing'an Range, NE China and its tectonic implications. Acta Petrologica Sinica, 29: 354–368.
Xu, W.L., Wang, F., Pei, F.P., Meng, E., Tang, J., Xu, M.J., and Wang, W., 2013b. Mesozoic tectonic regimes and regional ore -forming background in NE China: constraints from spatial and temporal variations of Mesozoic volcanic rock associations. Acta Petrologica Sinica, 29: 339–353.
Xu, W.L., Pei, F.P., Wang, F., Meng, E., Ji, W.Q., Yang, D.B., and Wang, W., 2013c. Spatial–temporal relationships of Mesozoic volcanic rocks in NE China: constraints on tectonic overprinting and transformations between multiple tectonic regimes. Journal of Asian Earth Sciences, 74: 167–193.
Xu, W.L., Ji, W.Q., Pei, F.P., Meng, E., Yu, Y., Yang, D.B., and Zhang, X.Z., 2009. Triassic volcanism in eastern Heilongjiang and Jilin provinces, NE China: chronology, geochemistry, and tectonic implications. Journal of Asian Earth Sciences, 34: 392–402.
Xu,W.L., Sun, C.Y., Tang, J., Luan, J.P., and Wang F., 2019. Basement Nature and Tectonic Evolution of the Xing'an-Mongolian Orogenic Belt. Earth sciences, http://kns.cnki.net/kcms/detail/42.1874.p.20190228.2155.014.html.
Yang, W.B., Niu, H.C., Shan, Q., Sun, W.D., Zhang, H., Li, N.B., Jiang, Y.H., and Yu, X.Y., 2014. Geochemistry of magmatic and hydrothermal zircon from the highly evolved Baerzhe alkaline granite: implications for Zr–REE–Nb mineralization. Mineralium Deposita, 49: 451–470.
Yang, W.B., Niu, H.C., Cheng, L.R., Shan, Q., and Li, N.B., 2015. Geochronology, geochemistry and geodynamic implications of the Late Mesozoic volcanic rocks in the southern Great Xing'an Mountains, NE China. Journal of Asian Earth Sciences, 113: 454–470.
Yang, X.L., 2007. Geological characteristics and study of detrital zircon geochronology of metamorphic rock series in Zhalantun area. Master Degree Thesis. Changchun: Jilin University (in Chinese with English abstract).
Zeng, L.J., Niu, H.C., Bao, Z.W., and Yang, W.B., 2017. Chemical lattice expansion of natural zircon during the magmatic-hydrothermal evolution of A-type granite. American Mineralogist, 102(3): 655–665.
Zhang, G.B., Ireland, T., Zhang, L.F., Gao, Z., and Song, S.G., 2016. Zircon geochemistry of two contrasting types of eclogite: Implications for the tectonic evolution of the North Qaidam UHPM belt, northern Tibet. Gondwana Research, 35: 27–39.
Zhang, C., Wu, X.W., Guo, W., Zhang, Y.J., Quan, J.Y., 2017. Discovery of the 1.8 Ga granite on the Western Margin of the Songnen Massif, China. Acta Geologica Sinica, 91: 1497–1498.
Zhou, J.B., Wilde, S.A., Zhang, X.Z., Zhao, G.C., Liu, F.L., and Qiao, D.W., 2011. A > 1300 km late pan-african metamorphic belt in ne china: new evidence from the Xing'an block and its tectonic implications. Tectonophysics, 509(3–4): 280–292.
Zhou, J.B., Wilde, S.A., Zhang, X.Z., Ren, S. M., and Zheng, C.Q. ,2011. Early paleozoic metamorphic rocks of the erguna block in the great xing"an range, NE China: evidence for the timing of magmatic and metamorphic events and their tectonic implications. Tectonophysics, 499(1-4): 105–117.
Zhou, J.B., and Wilde, S.A., 2013. The crustal accretion history and tectonic evolution of the ne china segment of the central asian orogenic belt. Gondwana Research, 23(4): 1365–1377.
Zhou, J.B., Wang, B., Zeng, W.S., and Cao, J.L., 2014. Detrital zircon U-Pb dating of the zhalantun metamorphic complex and its tectonic implications, great xing' an, ne china. Acta Petrologica Sinica, 30: 1879–1888.

About the first author

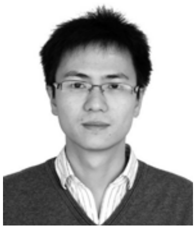

QIN Tao, male, born in 1985 in Suining City, Sichuan Province; Doctor; graduated from Jilin University; Engineer of Shenyang Geological Survey Center. He is now interested in the study on the Paleozoic to Mesozoic magmatic and tectonic events of the Great Khingan. Email: qintao2008@hotmail. com; phone: 024-81847131, 18940276788.

About the corresponding author

GUO Rongrong, female, born in 1989 in the Zhoukou, Henan Province; Doctor, graduated from the Peking University; Associated professor of the Department of Geology, Key Laboratory of Ministry of Education on Safe Mining of Deep Metal Mines, School of Resources and Civil Engineering, Northeastern University. She is now interested in the study on the Precambrian Geology and geochemistry. Email: guorongrong@mail.neu.edu.cn; Phone: 18041342200.